Controlling quantum-dot light absorption and emission by a surface-plasmon field

Danhong Huang,[1*] Michelle Easter,[2] Godfrey Gumbs,[3] A. A. Maradudin,[4] Shawn-Yu Lin,[5] D. A. Cardimona,[1] and Xiang Zhang[6]

[1]*Air Force Research Laboratory, Space Vehicles Directorate, Kirtland Air Force Base, New Mexico 87117, USA*
[2]*Department of Mechanical Engineering, Stevens Institute of Technology, 1 Castle Point Terrace, Hoboken, New Jersey 07030, USA*
[3]*Department of Physics and Astronomy, Hunter College of the City University of New York, 695 Park Avenue New York, New York 10065, USA*
[4]*Department of Physics and Astronomy, University of California, Irvine, California 92697, USA*
[5]*Department of Electrical, Computer and Systems Engineering, Rensselaer Polytechnic Institute, 110 8th Street, Troy, New York 12180, USA*
[6]*Department of Mechanical Engineering, 3112 Etcheverry Hall, University of California at Berkeley, Berkeley, California 94720, USA*
[*]*danhong.huang@us.af.mil*

Abstract: The possibility for controlling both the probe-field optical gain and absorption, as well as photon conversion by a surface-plasmon-polariton near field is explored for a quantum dot located above a metal surface. In contrast to the linear response in the weak-coupling regime, the calculated spectra show an induced optical gain and a triply-split spontaneous emission peak resulting from the interference between the surface-plasmon field and the probe or self-emitted light field in such a strongly-coupled nonlinear system. Our result on the control of the mediated photon-photon interaction, very similar to the 'gate' control in an optical transistor, may be experimentally observable and applied to ultra-fast intrachip/interchip optical interconnects, improvement in the performance of fiber-optic communication networks, and developments of optical digital computers and quantum communications.

OCIS codes: (250.5590) Quantum-well, -wire and -dot devices; (250.5403) Plasmonics; (290.5838) Scattering, in-field; (160.4760) Optical properties.

References and links

1. O. Firstenberg, T. Peyronel, Q.-Y. Liang, A. V. Gorshkov, M. D. Lukin, and V. Vuletić, "Attractive photons in a quantum nonlinear medium," Nat. **502**, 71–75 (2013).
2. S. Schmitt-Rink, D. S. Chemla, and H. Haug, "Nonequilibrium theory of the optical Stark effect and spectral hole burning in semiconductors," Phys. Rev. B **37**, 941–955 (1988).
3. I. Fushman, D. Englund, A. Faraon, N. Stoltz, P. Petroff, and J. Vučković, "Controlled phase shifts with a single quantum dot," Sci. **320**, 769–772 (2008).
4. W. Chen, K. M. Beck, R. Bücker, M. Gullans, M. D. Lukin, H. Tanji-Suzuki, and V. Vuletić, "All-optical switch and transistor gated by one stored photon," Sci. **341**, 768–770 (2013).

#217702 - $15.00 USD Received 23 Jul 2014; accepted 16 Sep 2014; published 30 Oct 2014

5. G. Gumbs and D. H. Huang, *Properties of Interacting Low-Dimensional Systems* (Wiley-VCH Verlag GmbH & Co. kGaA, 2011), Chaps. 4, 5.
6. D. H. Huang, G. Gumbs, and S.-Y. Lin, "Self-consistent theory for near-field distribution and spectrum with quantum wires and a conductive grating in terahertz regime," J. Appl. Phys. **105**, 093715 (2009).
7. D. Dini, R. Köhler, A. Tredicucci, G. Biasiol, and L. Sorba, "Microcavity polariton splitting of intersubband transitions," Phys. Rev. Lett. **90**, 116401 (2003).
8. Y. Todorov, A. M. Andrews, I. Sagnes, R. Colombelli, P. Klang, G. Strasser, and C. Sirtori, "Strong light-matter coupling in subwavelength metal-dielectric microcavities at terahertz frequencies," Phys. Rev. Lett. **102**, 186402 (2009).
9. Y. Todorov, A. M. Andrews, R. Colombelli, S. De Liberato, C. Ciuti, P. Klang, G. Strasser, and C. Sirtori, "Ultrastrong light-matter coupling regime with polariton dots," Phys. Rev. Lett. **105**, 196402 (2010).
10. H. Deng, H. Haug, and Y. Yamamoto, "Exciton-polariton Bose-Einstein condensation," Rev. Mod. Phys. **82**, 1489–1537 (2010).
11. S. Christopoulos, G. B. H. von Högersthal, A. J. D. Grundy, P. G. Lagoudakis, A.V. Kavokin, J. J. Baumberg, G. Christmann, R. Butté, E. Feltin, J.-F. Carlin, and N. Grandjean, "Room-temperature polariton lasing in semiconductor microcavities," Phys. Rev. Lett. **98**, 126405 (2007).
12. S. I. Tsintzos, N. T. Pelekanos, G. Konstantinidis, Z. Hatzopoulos, and P. G. Savvidis, "A GaAs polariton light-emitting diode operating near room temperature," Nat. Lett. **453**, 372–375 (2008).
13. P. Bhattacharya, B. Xiao, A. Das, S. Bhowmick, and J. Heo, "Solid state electrically injected exciton-polariton laser," Phys. Rev. Lett. **110**, 206403 (2013).
14. C. Schneider, A. Rahimi-Iman, N. Y. Kim, J. Fischer, I. G. Savenko, M. Amthor, M. Lermer, A. Wolf, L. Worschech, V. D. Kulakovskii, I. A. Shelykh, M. Kamp, S. Reitzenstein, A. Forchel, Y. Yamamoto, and S. Höfling, "An electrically pumped polariton laser," Nat. **497**, 348–352 (2013).
15. F. Jahnke, M. Kira, and S. W. Koch, "Linear and nonlinear optical properties of excitons in semiconductor quantum wells and microcavities," Z. Phys. B **104**, 559–572 (1997).
16. D. H. Huang, M. M. Easter, G. Gumbs, A. A. Maradudin, S.-Y. Lin, D. A. Cardimona, and X. Zhang, "Resonant scattering of surface plasmon polaritons by dressed quantum dots," Appl. Phys. Lett. **104**, 251103 (2014).
17. Y. H. Cao, J. Xie, Y. M. Liu, and Z. Y. Liu, "Modeling and optimization of photonic crystal devices based on transformation optics method," Opt. Express **22**, 2725–2734 (2014).
18. X. Yang, J. Yao, J. Rho, X. Yin, and X. Zhang, "Experimental realization of three-dimensional indefinite cavities at the nanoscale with anomalous scaling laws," Nat. Photonics **6**, 450–454 (2012).
19. M. Lindberg, Y. Z. Hu, R. Binder, and S. W. Koch, "$\chi^{(3)}$ formalism in optically excited semiconductors and its applications in four-wave-mixing spectroscopy," Phys. Rev. B **50**, 18060–18072 (1994).
20. D. H. Huang and P. M. Alsing, "Many-body effects on optical carrier cooling in intrinsic semiconductors at low lattice temperatures," Phys. Rev. B **78**, 035206 (2008).
21. H. M. Gibbs, G. Khitrova, and S. W. Koch, "Exciton-polariton light-semiconductor coupling effects," Nat. Photonics **5**, 275–282 (2011).
22. T. Yoshie, A. Scherer, J. Hendrickson, G. Khitrova, H. M. Gibbs, G. Rupper, C. Ell, O. B. Shchekin, and D. G. Deppe, "Vacuum Rabi splitting with a single quantum dot in a photonic crystal nanocavity," Nat. **432**, 200–203 (2004).
23. R. F. Oulton, V. J. Sorger, T. Zentgraf, R.-M. Ma, C. Gladden, L. Dai, G. Bartal, and X. Zhang, "Plasmon lasers at deep subwavelength scale," Nat. Lett. **461**, 629–632 (2009).
24. F. Alpeggiani, S. D'Agostino, and L. C. Andreani, "Surface plasmons and strong light-matter coupling in metallic nanoshells," Phys. Rev. B **86**, 035421 (2012).
25. A. A. Maradudin and D. L. Mills, "Scattering and absorption of electromagnetic radiation by a semi-infinite medium in the presence of surface roughness," Phys. Rev. B **11**, 1392–1415 (1975).
26. M. G. Cottam and A. A. Maradudin, "Surface linear response functions," in *Surface Excitations*, eds. V. M. Agranovich and R. Loudon (North-Holland, Amsterdam, 1984), pp. 1–194.
27. R. V. Shenoi, J. Bur, D. H. Huang, and S.-Y. Lin, "Extraordinary plasmon-QD interaction for enhanced infrared application," Proc. SPIE **8632**, Photonic and Phononic Properties of Engineered Nanostructures III, 86321L (2013).
28. R. V. Shenoi, S.-Y. Lin, S. Krishna, and D. H. Huang, "Order-of-magnitude enhancement of intersubband photoresponse in a plasmonic-quantum dot system," Opt. Lett. **39**, 4454–4457 (2014).
29. M. S. Tame, K. R. McEnery, S. K. Özdemir, J. Lee, S. A. Maier, and M. S. Kim, "Quantum plasmonics," Nat. Phys. **9**, 329–340 (2013).
30. F. Rossi and T. Kuhn, "Theory of ultrafast phenomena in photoexcited semiconductors," Rev. Mod. Phys. **74**, 895–950 (2002).
31. V. M. Axt and T. Kuhn, "Femtosecond spectroscopy in semiconductors: a key to coherences, correlations and quantum kinetics," Rep. Prog. Phys. **67**, 433–512 (2004).
32. M. Kira and S. W. Koch, "Many-body correlations and excitonic effects in semiconductor spectroscopy," Prog. Quant. Electr. **30**, 155–296 (2006).
33. D. H. Huang , P. M. Alsing, T. Apostolova, and D. A. Cardimona, "Coupled energy-drift and force-balance

#217702 - $15.00 USD Received 23 Jul 2014; accepted 16 Sep 2014; published 30 Oct 2014

equations for high-field hot-carrier transport," Phys. Rev. B **71**, 195205 (2005).
34. D. H. Huang and D. A. Cardimona, "Intersubband laser coupled three-level asymmetric quantum wells: new dynamics of quantum interference," J. Opt. Soc. Am. B **15**, 1578—1584 (1998).
35. E. O. Kane, "Band structure of indium antimonide," J. Physi. Chem. Solids **1**, 249–261 (1957).
36. U. Bockelmann and G. Bastard, "Interband absorption in quantum wires. I. Zero-magnetic-field case," Phys. Rev. B **45**, 1688–1699 (1992).

1. Introduction

It is well known that photons inherently do not interact with each other. In classical electrodynamics, Maxwell equations are linear and cannot describe any photon-photon interaction. However, effective photon-photon coupling could exist in a mediated way, e.g., through their interactions with matter. Very recently, an experiment [1], which involves firing pairs of photons through an ultra-cold atomic gas, provided the evidence for an attractive interaction between photons to form so-called 'molecules' of light. In general, if the interaction between photons and matter is strong, the optical response of matter will become nonlinear and the resulting bandedge optical nonlinearities [2] will enable an effective photon-photon interaction [3]. An optical transistor [4] could be based on this idea, where 'gate' photons control the intensity of a light beam 'source'. Optical transistors could be applied to speed up and improve the performance of fiber-optic communication networks. Here, all-optical digital signal processing and routing is fulfilled by arranging optical transistors in photonic integrated circuits, and the signal loss during the propagation could be compensated by inserting new types of optical amplifiers. Moreover, optical transistors are expected to play an important role in the development of an optical digital computer or quantum-encrypted communication.

Most previous research on optical properties of materials, including optical absorption, inelastic light scattering, and spontaneous emission, used a weak probe field as a perturbation to the studied system [5]. In this weak-coupling regime, the optical response of electrons depends only on the material characteristics [6], and, therefore, no photon-photon interaction is expected. However, the strong-coupling regime could be reached with help from microcavities, and the experimental effort on searching for polariton condensation (resulting from strong light-electron interaction) in semiconductors continues to produce results [7–9]. A general review of exciton-polariton condensation may be found in [10]. Successful demonstration of room-temperature polariton lasing without population inversion in semiconductor microcavities using both optical pumping [11, 12] and electrical injection [13, 14] have made it possible to achieve ultra-low lasing thresholds and very small emitter sizes comparable to the emitted wavelength. Semiconductor exciton-polariton nanolasers could advance intrachip and interchip optical interconnects by integrating them into semiconductor-based photonic chips. They might also have applications in medical devices and treatments, such as spatially selective illumination of individual neuron cells to locally control neuron firing activities in optogenetics and neuroscience, and near-field high-resolution imaging beyond the optical diffraction limit as well.

Theoretically, a big hurdle also exists for studying photon-photon interactions in the strong-coupling regime mainly due to intractable numerical calculations for systems with very strong nonlinearity. The existence of strong nonlinearity in such a system means that any perturbative theories, e.g. using bare electron states or linear response theory [5], become inadequate for describing both field and electron dynamics in this system. The presence of an induced polarization, regarded as a source term in Maxwell equations [15, 16], from photo-excited electrons makes it impossible for us to solve the field equations by simply using finite-element analysis [17] or finite-difference-time-domain methods [18]. Although the semiconductor-Bloch equations [19] and density-matrix equations [5, 20], derived from many-body theory, are able to accurately capture the nonlinear optical response of electrons, the inclusion of pair scatte-

#217702 - $15.00 USD Received 23 Jul 2014; accepted 16 Sep 2014; published 30 Oct 2014

ring effects on both energy relaxation and optical dephasing precludes an analytic approach for seeking a solution of these equations. Consequently, there exist only very few theoretical studies on resonantly-coupled excitons to microcavity field [21], which depend heavily on computer simulations, and focus on simplified one-dimensional strongly-coupled microcavity systems.

Physically, not only high-quality microcavities [22] but also intense surface-plasmon near fields [23, 24] should be employed for reaching the strong-coupling goal in semiconductors. In this paper, we solve the self-consistent equations for strongly-coupled electromagnetic-field dynamics and electron quantum kinetics in a quantum dot above the surface of a thick metallic film. This is a situation that has not been fully explored so far from either a theoretical or experimental point of view. This is done based on finding an analytical solution to Green's function [25,26] for a quantum dot coupled to a semi-infinite metallic material system, which makes it easy to calculate the effect of the induced polarization field as a source term in Maxwell equations. In our formalism, the strong light-electron interaction is reflected in the photon-dressed electronic states with a Rabi gap and in the feedback from the induced optical polarization of dressed electrons to the incident light. The formalism derived in this paper goes beyond the weak-coupling limit and deals with a much more realistic structure in the strong-coupling limit for the development of a surface-plasmon polariton laser with a very low threshold pumping. Our results clearly demonstrate the ability to *control probe-field optical gain and absorption, and photon conversion* by a surface-plasmon field with temperature-driven frequency detuning in such a nonlinear system led by dressed electron states, very similar to the 'gate' control in an optical transistor. These conclusions should be experimentally observable [27,28]. On the other hand, our numerical results also provide an example that demonstrates the so-called quantum plasmonics [29], where the properties of surface-plasmon polaritons and quantum-confined electrons are hybridized through near-field coupling.

In Sec. 2, we introduce our physics model and derive self-consistent equations for determining the coupled scattering dynamics of a surface-plasmon field and the quantum kinetics of electrons in quantum dots. Section 3 is devoted to a full discussion of our numerical results, including scattering and optical absorption of the surface-plasmon-polariton field by quantum dots, spontaneous emission, and the nonlinear optical response of the dressed electron states. Some concluding remarks are given in Sec. 4.

2. Model and theory

Our model system, as shown in Fig. 1, consists of a semi-infinite metallic material with a semiconductor quantum dot above its surface. A surface-plasmon-polariton (SPP) field is locally excited through a surface grating by normally-incident light. This propagating SPP field further excites an interband electron-hole (e-h) plasma in the quantum dot. The induced optical-polarization field of the photo-excited e-h plasma is strongly coupled to the SPP field to produce split degenerate e-h plasma and SPP modes with an anticrossing gap. A brief description of our self-consistent formalism was reported earlier [16]. In order to let readers follow easily the details of our model and formalism, we present here the full derivation of the Maxwell-Bloch numerical approach for an SPP field coupled to a photo-excited e-h plasma in the quantum dot.

2.1. General formalism

The Maxwell equation for a semi-infinite non-magnetic medium in position-frequency space can be written as [25]

$$\nabla\times\nabla\times E(\mathbf{r};\omega)-\varepsilon_{\mathrm{b}}(x_3;\omega)\,\frac{\omega^2}{c^2}\,E(\mathbf{r};\omega)=\frac{\omega^2}{\varepsilon_0 c^2}\,\mathscr{P}^{\mathrm{loc}}(\mathbf{r};\omega)\ , \tag{1}$$

#217702 - $15.00 USD Received 23 Jul 2014; accepted 16 Sep 2014; published 30 Oct 2014

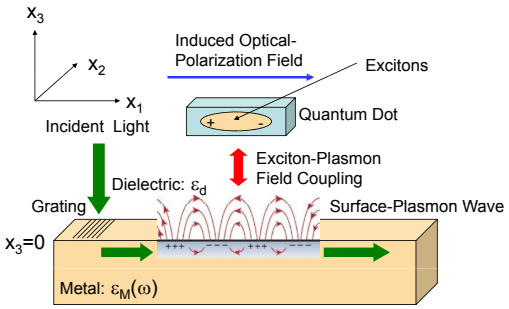

Fig. 1. Schematic illustration for a semi-infinite metal and a quantum dot above its surface at $x_3 = 0$. Here, the surface-plasmon polariton (SPP) is locally excited by incident light with the help of a surface grating. The propagating SPP field further excites e-h pairs (plasmas) in the adjacent quantum dot. As a result, the optical-polarization field of the photo-excited e-h plasma is strongly coupled to the propagating SPP field to form split plasma-SPP modes with an anticrossing gap. Also, a probe-field is used for studying the photon dressing effect.

where $E(\mathbf{r};\omega)$ is the electric component of an electromagnetic field, $H(\mathbf{r};\omega) = -\left(\frac{i}{\omega\mu_0}\right)\nabla\times E(\mathbf{r};\omega)$ is the magnetic component of the electromagnetic field, $\mathbf{r} = (x_1, x_2, x_3)$ is a three-dimensional position vector, ω is the angular frequency of the incident light, ε_0, μ_0 and c are the permittivity, permeability and speed of light in vacuum, $\mathscr{P}^{\rm loc}(\mathbf{r};\omega)$ is an off-surface local polarization field generated by optical transitions of electrons in a quantum dot, and the position-dependent dielectric function is

$$\varepsilon_{\rm b}(x_3;\omega) = \begin{cases} \varepsilon_{\rm d}\,, & \text{for } x_3 > 0 \\ \varepsilon_{\rm M}(\omega)\,, & \text{for } x_3 < 0 \end{cases} . \tag{2}$$

Here, $\varepsilon_{\rm d}$ characterizes for the semi-infinite dielectric material in the region $x_3 > 0$, while $\varepsilon_{\rm M}(\omega)$ is the dielectric function of the semi-infinite metallic material in the region $x_3 < 0$. For the Maxwell equation in Eq. (1), we introduce the Green's function $\mathscr{G}_{\mu\nu}(\mathbf{r},\mathbf{r}';\omega)$ that satisfies the following equation

$$\sum_{\mu}\left[\varepsilon_{\rm b}(x_3;\omega)\,\frac{\omega^2}{c^2}\,\delta_{\lambda\mu} - \frac{\partial^2}{\partial x_\lambda \partial x_\mu} + \delta_{\lambda\mu}\,\nabla^2_{\mathbf{r}}\right]\mathscr{G}_{\mu\nu}(\mathbf{r},\mathbf{r}';\omega) = \delta_{\lambda\nu}\,\delta(\mathbf{r}-\mathbf{r}')\,, \tag{3}$$

where $\nabla^2_{\mathbf{r}} = \sum_{\mu}\frac{\partial^2}{\partial x_\mu^2}$ is the Laplace operator, $\delta_{\lambda\mu}$ represents the Kronecker delta, and the indices $\lambda, \mu = 1, 2, 3$ indicate three spatial directions. Using the Green's function defined in Eq. (3), we can convert the Maxwell equation in Eq. (1) into a three-dimensional integral equation

$$E_\mu(\mathbf{r};\omega) = E^{(0)}_\mu(\mathbf{r};\omega) - \frac{\omega^2}{\varepsilon_0 c^2}\sum_{\nu}\int d^3\mathbf{r}'\,\mathscr{G}_{\mu\nu}(\mathbf{r},\mathbf{r}';\omega)\,\mathscr{P}^{\rm loc}_\nu(\mathbf{r}';\omega)\,, \tag{4}$$

where $E^{(0)}_\mu(\mathbf{r};\omega)$ is a solution of the corresponding homogeneous equation

$$\sum_{\nu}\left[\varepsilon_{\rm b}(x_3;\omega)\,\frac{\omega^2}{c^2}\,\delta_{\mu\nu} - \frac{\partial^2}{\partial x_\mu \partial x_\nu} + \delta_{\mu\nu}\,\nabla^2_{\mathbf{r}}\right]E^{(0)}_\nu(\mathbf{r};\omega) = 0\,, \tag{5}$$

and the source term $\mathscr{P}^{\rm loc}_\nu(\mathbf{r}';\omega)$ generally depends on the electric field in a nonlinear way and can be determined by the Bloch equation [2, 15].

#217702 - $15.00 USD Received 23 Jul 2014; accepted 16 Sep 2014; published 30 Oct 2014

2.2. Solving for Green's function

For a semi-infinite medium, the Green's function can be formally expressed by its Fourier transform

$$\mathscr{G}_{\mu\nu}(\mathbf{r},\mathbf{r}';\omega)=\int\frac{d^2\mathbf{k}_\parallel}{(2\pi)^2}\,e^{i\mathbf{k}_\parallel\cdot(\mathbf{r}_\parallel-\mathbf{r}'_\parallel)}\,g_{\mu\nu}(\mathbf{k}_\parallel,\omega|x_3,x'_3)\;, \tag{6}$$

where we have introduced the two-dimensional vectors $\mathbf{r}_\parallel=(x_1,x_2)$ and $\mathbf{k}_\parallel=(k_1,k_2)$. Substituting Eq. (6) into Eq. (3), we obtain

$$\begin{bmatrix} \varepsilon_b\dfrac{\omega^2}{c^2}-k_2^2+\dfrac{d^2}{dx_3^2} & k_1k_2 & -ik_1\dfrac{d}{dx_3} \\ k_1k_2 & \varepsilon_b\dfrac{\omega^2}{c^2}-k_1^2+\dfrac{d^2}{dx_3^2} & -ik_2\dfrac{d}{dx_3} \\ -ik_1\dfrac{d}{dx_3} & -ik_2\dfrac{d}{dx_3} & \varepsilon_b\dfrac{\omega^2}{c^2}-k_\parallel^2 \end{bmatrix}\begin{bmatrix} g_{11} & g_{12} & g_{13} \\ g_{21} & g_{22} & g_{23} \\ g_{31} & g_{32} & g_{33} \end{bmatrix}$$
$$=\delta(x_3-x'_3)\begin{bmatrix} 1 & 0 & 0 \\ 0 & 1 & 0 \\ 0 & 0 & 1 \end{bmatrix}. \tag{7}$$

After a rotational transformation [25] is performed in $\mathbf{k}_\parallel$-space, i.e.,

$$f_{\mu\nu}(k_\parallel,\omega|x_3,x'_3)=\sum_{\mu',\nu'}\mathscr{S}_{\mu\mu'}(\mathbf{k}_\parallel)\,\mathscr{S}_{\nu\nu'}(\mathbf{k}_\parallel)\,g_{\mu'\nu'}(\mathbf{k}_\parallel,\omega|x_3,x'_3)\;, \tag{8}$$

where the rotational matrix $\mathscr{S}(\mathbf{k}_\parallel)$ is

$$\mathscr{S}(\mathbf{k}_\parallel)=\frac{1}{k_\parallel}\begin{bmatrix} k_1 & k_2 & 0 \\ -k_2 & k_1 & 0 \\ 0 & 0 & k_\parallel \end{bmatrix}, \tag{9}$$

we acquire an equivalent version of Eq. (7)

$$\begin{bmatrix} \varepsilon_b\dfrac{\omega^2}{c^2}+\dfrac{d^2}{dx_3^2} & 0 & -ik_\parallel\dfrac{d}{dx_3} \\ 0 & \varepsilon_b\dfrac{\omega^2}{c^2}-k_\parallel^2+\dfrac{d^2}{dx_3^2} & 0 \\ -ik_\parallel\dfrac{d}{dx_3} & 0 & \varepsilon_b\dfrac{\omega^2}{c^2}-k_\parallel^2 \end{bmatrix}\begin{bmatrix} f_{11} & f_{12} & f_{13} \\ f_{21} & f_{22} & f_{23} \\ f_{31} & f_{32} & f_{33} \end{bmatrix}$$
$$=\delta(x_3-x'_3)\begin{bmatrix} 1 & 0 & 0 \\ 0 & 1 & 0 \\ 0 & 0 & 1 \end{bmatrix}. \tag{10}$$

To obtain the solution of Eq. (10), we need to employ both the finite-value boundary condition at $x'_3=\pm\infty$ and the continuity boundary condition at the $x_3=0$ interface. This leads to the following five non-zero $f_{\mu\nu}(k_\parallel,\omega|x_3,x'_3)$ elements [25, 26]:

$$f_{22}(k_\parallel,\omega|x_3,x'_3)$$

#217702 - $15.00 USD Received 23 Jul 2014; accepted 16 Sep 2014; published 30 Oct 2014

$$= \begin{cases} -\left(\frac{i}{2p}\right)\frac{2p}{p_\mathrm{d}+p}\, e^{ip_\mathrm{d}x_3 - ipx_3'}\,, & x_3>0\,,\, x_3'<0 \\ -\left(\frac{i}{2p}\right)\left[e^{ip|x_3-x_3'|} - \frac{p_\mathrm{d}-p}{p_\mathrm{d}+p}\, e^{-ip(x_3+x_3')}\right], & x_3<0\,,\, x_3'<0 \\ -\left(\frac{i}{2p_\mathrm{d}}\right)\left[e^{ip_\mathrm{d}|x_3-x_3'|} + \frac{p_\mathrm{d}-p}{p_\mathrm{d}+p}\, e^{ip_\mathrm{d}(x_3+x_3')}\right], & x_3>0\,,\, x_3'>0 \\ -\left(\frac{i}{2p_\mathrm{d}}\right)\frac{2p_\mathrm{d}}{p_\mathrm{d}+p}\, e^{-ip(x_3-x_3')}\,, & x_3<0\,,\, x_3'>0 \end{cases}, \tag{11}$$

$f_{13}(k_\parallel,\omega|x_3,x_3')$

$$= \begin{cases} \frac{ik_\parallel c^2}{2\varepsilon_\mathrm{M}(\omega)\omega^2}\left[\frac{2\varepsilon_\mathrm{M}(\omega)p_\mathrm{d}}{\varepsilon_\mathrm{M}(\omega)p_\mathrm{d}+\varepsilon_\mathrm{d}\,p}\right] e^{ip_\mathrm{d}x_3 - ipx_3'}\,, & x_3>0\,,\, x_3'<0 \\ \frac{ik_\parallel c^2}{2\varepsilon_\mathrm{M}(\omega)\omega^2}\left[e^{ip|x_3-x_3'|}\,\mathrm{sgn}(x_3-x_3') + \frac{\varepsilon_\mathrm{M}(\omega)p_\mathrm{d}-\varepsilon_\mathrm{d}\,p}{\varepsilon_\mathrm{M}(\omega)p_\mathrm{d}+\varepsilon_\mathrm{d}\,p}\, e^{-ip(x_3+x_3')}\right], & x_3<0\,,\, x_3'<0 \\ \frac{ik_\parallel c^2}{2\varepsilon_\mathrm{d}\,\omega^2}\left[e^{ip_\mathrm{d}|x_3-x_3'|}\,\mathrm{sgn}(x_3-x_3') + \frac{\varepsilon_\mathrm{M}(\omega)p_\mathrm{d}-\varepsilon_\mathrm{d}\,p}{\varepsilon_\mathrm{M}(\omega)p_\mathrm{d}+\varepsilon_\mathrm{d}\,p}\, e^{ip_\mathrm{d}(x_3+x_3')}\right], & x_3>0\,,\, x_3'>0 \\ -\frac{ik_\parallel c^2}{2\varepsilon_\mathrm{d}\,\omega^2}\left[\frac{2\varepsilon_\mathrm{d}\,p}{\varepsilon_\mathrm{M}(\omega)p_\mathrm{d}+\varepsilon_\mathrm{d}\,p}\right] e^{-ipx_3+ip_\mathrm{d}x_3'}\,, & x_3<0\,,\, x_3'>0 \end{cases} \tag{12}$$

$f_{33}(k_\parallel,\omega|x_3,x_3')$

$$= \begin{cases} -\frac{ik_\parallel^2 c^2}{\omega^2}\left[\frac{1}{\varepsilon_\mathrm{M}(\omega)p_\mathrm{d}+\varepsilon_\mathrm{d}\,p}\right] e^{ip_\mathrm{d}x_3 - ipx_3'}\,, & x_3>0\,,\, x_3'<0 \\ \frac{c^2}{\varepsilon_\mathrm{M}(\omega)\omega^2}\,\delta(x_3-x_3') - \frac{ik_\parallel^2 c^2}{2p\,\varepsilon_\mathrm{M}(\omega)\omega^2}\left[e^{ip|x_3-x_3'|} - \frac{\varepsilon_\mathrm{M}(\omega)p_\mathrm{d}-\varepsilon_\mathrm{d}\,p}{\varepsilon_\mathrm{M}(\omega)p_\mathrm{d}+\varepsilon_\mathrm{d}\,p}\, e^{-ip(x_3+x_3')}\right], & x_3<0\,,\, x_3'<0 \\ \frac{c^2}{\varepsilon_\mathrm{d}\,\omega^2}\,\delta(x_3-x_3') - \frac{ik_\parallel^2 c^2}{2p_\mathrm{d}\varepsilon_\mathrm{d}\,\omega^2}\left[e^{ip_\mathrm{d}|x_3-x_3'|} + \frac{\varepsilon_\mathrm{M}(\omega)p_\mathrm{d}-\varepsilon_\mathrm{d}\,p}{\varepsilon_\mathrm{M}(\omega)p_\mathrm{d}+\varepsilon_\mathrm{d}\,p}\, e^{ip_\mathrm{d}(x_3+x_3')}\right], & x_3>0\,,\, x_3'>0 \\ -\frac{ik_\parallel^2 c^2}{\omega^2}\left[\frac{1}{\varepsilon_\mathrm{M}(\omega)p_\mathrm{d}+\varepsilon_\mathrm{d}\,p}\right] e^{-ipx_3+ip_\mathrm{d}x_3'}\,, & x_3<0\,,\, x_3'>0 \end{cases} \tag{13}$$

$f_{11}(k_\parallel,\omega|x_3,x_3')$

#217702 - $15.00 USD Received 23 Jul 2014; accepted 16 Sep 2014; published 30 Oct 2014

$$= \begin{cases} -\dfrac{ip_{\rm d}pc^2}{\omega^2}\left[\dfrac{1}{\varepsilon_{\rm M}(\omega)p_{\rm d}+\varepsilon_{\rm d}p}\right]e^{ip_{\rm d}x_3-ipx_3'}\,, & x_3>0\,,\,x_3'<0 \\ -\dfrac{ipc^2}{2\varepsilon_{\rm M}(\omega)\omega^2}\left[e^{ip|x_3-x_3'|}+\dfrac{\varepsilon_{\rm M}(\omega)p_{\rm d}-\varepsilon_{\rm d}p}{\varepsilon_{\rm M}(\omega)p_{\rm d}+\varepsilon_{\rm d}p}\,e^{-ip(x_3+x_3')}\right], & x_3<0\,,\,x_3'<0 \\ -\dfrac{ip_{\rm d}c^2}{2\varepsilon_{\rm d}\omega^2}\left[e^{ip_{\rm d}|x_3-x_3'|}-\dfrac{\varepsilon_{\rm M}(\omega)p_{\rm d}-\varepsilon_{\rm d}p}{\varepsilon_{\rm M}(\omega)p_{\rm d}+\varepsilon_{\rm d}p}\,e^{ip_{\rm d}(x_3+x_3')}\right], & x_3>0\,,\,x_3'>0 \\ -\dfrac{ip_{\rm d}c^2}{2\varepsilon_{\rm d}\omega^2}\left[\dfrac{2\varepsilon_{\rm d}p}{\varepsilon_{\rm M}(\omega)p_{\rm d}+\varepsilon_{\rm d}p}\right]e^{-ipx_3+ip_{\rm d}x_3'}\,, & x_3<0\,,\,x_3'>0 \end{cases} \tag{14}$$

$$f_{31}(k_\parallel,\omega|x_3,x_3')$$

$$= \begin{cases} \dfrac{ik_\parallel c^2}{\omega^2}\left[\dfrac{p}{\varepsilon_{\rm M}(\omega)p_{\rm d}+\varepsilon_{\rm d}p}\right]e^{ip_{\rm d}x_3-ipx_3'}\,, & x_3>0\,,\,x_3'<0 \\ \dfrac{ik_\parallel c^2}{2\varepsilon_{\rm M}(\omega)\omega^2}\left[e^{ip|x_3-x_3'|}\,\mathrm{sgn}(x_3-x_3')-\dfrac{\varepsilon_{\rm M}(\omega)p_{\rm d}-\varepsilon_{\rm d}p}{\varepsilon_{\rm M}(\omega)p_{\rm d}+\varepsilon_{\rm d}p}\,e^{-ip(x_3+x_3')}\right], & x_3<0\,,\,x_3'<0 \\ \dfrac{ik_\parallel c^2}{2\varepsilon_{\rm d}\omega^2}\left[e^{ip_{\rm d}|x_3-x_3'|}\,\mathrm{sgn}(x_3-x_3')-\dfrac{\varepsilon_{\rm M}(\omega)p_{\rm d}-\varepsilon_{\rm d}p}{\varepsilon_{\rm M}(\omega)p_{\rm d}+\varepsilon_{\rm d}p}\,e^{ip_{\rm d}(x_3+x_3')}\right], & x_3>0\,,\,x_3'>0 \\ -\dfrac{ik_\parallel c^2}{\omega^2}\left[\dfrac{p_{\rm d}}{\varepsilon_{\rm M}(\omega)p_{\rm d}+\varepsilon_{\rm d}p}\right]e^{-ipx_3+ip_{\rm d}x_3'}\,, & x_3<0\,,\,x_3'>0 \end{cases} \tag{15}$$

where $\mathrm{sgn}(x)$ is the sign function,

$$p_{\rm d}(k_\parallel,\omega)=\sqrt{\varepsilon_{\rm d}\,\frac{\omega^2}{c^2}-k_\parallel^2}\,, \tag{16}$$

$$p(k_\parallel,\omega)=\sqrt{\varepsilon_{\rm M}(\omega)\,\frac{\omega^2}{c^2}-k_\parallel^2}\,, \tag{17}$$

$\mathrm{Im}[p_{\rm d}(k_\parallel,\omega)]\geq 0$ and $\mathrm{Im}[p(k_\parallel,\omega)]\geq 0$. In addition, from these non-zero $f_{\mu\nu}(k_\parallel,\omega|x_3,x_3')$ functions, we obtain

$$g_{\mu\nu}(\mathbf{k}_\parallel,\omega|x_3,x_3')=\sum_{\mu',\nu'}f_{\mu'\nu'}(k_\parallel,\omega|x_3,x_3')\,\mathscr{S}_{\mu'\mu}(\mathbf{k}_\parallel)\,\mathscr{S}_{\nu'\nu}(\mathbf{k}_\parallel)\,, \tag{18}$$

which can be substituted into Eq. (6) to calculate the Green's function $\mathscr{G}_{\mu\nu}(\mathbf{r},\mathbf{r}';\omega)$ in position space.

2.3. Local polarization field

In order to find the explicit field dependence in $\mathscr{P}^{\rm loc}(\mathbf{r};\omega)$, we now turn to the study of electron dynamics in a quantum dot. Here, the optical-polarization field $\mathscr{P}^{\rm loc}(\mathbf{r};\omega)$ plays a unique role on bridging the classical Maxwell equations for electromagnetic fields to the quantum-mechanical Schrödinger equation for electrons. The electron dynamics in photo-excited quantum dots can be described quantitatively by the so-called semiconductor Bloch equations [30–32]. These generalize the well-known optical Bloch equations in two aspects

#217702 - $15.00 USD Received 23 Jul 2014; accepted 16 Sep 2014; published 30 Oct 2014

including the incorporation of electron scattering with impurities, phonons and other electrons as well as many-body effects on dephasing in the photo-induced optical coherence.

The physical system considered in this paper is illustrated in Fig. 2, where we assume two levels for electrons and holes, respectively, in a quantum dot. These two energy levels of both electrons and holes are efficiently coupled by phonon scattering at high temperatures. Additionally, the lowest electron and hole energy levels are optically coupled to each other by an incident SPP field to form the dressed states of excitons. The SPP-controlled optical properties of quantum-dot excitons can either probed by a plane-wave field or seen from the spontaneous emission of excitons.

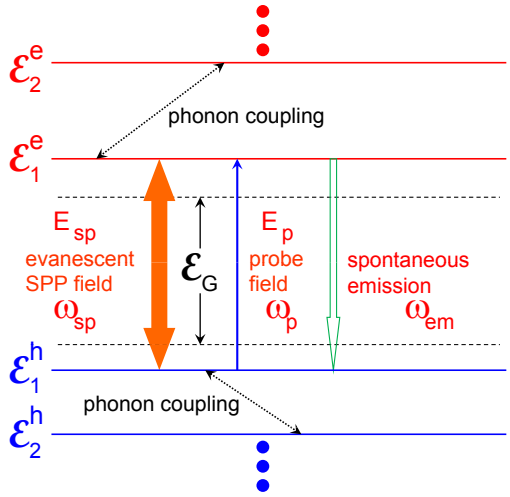

Fig. 2. Schematic illustration for a system incorporating the generation of quantum-dot excitons by a SPP field with frequency $\omega_{\rm sp}$ and probed by a plane-wave field E_p with frequency ω_p. Here, $\mathscr{E}_{\rm G}$ is the energy bandgap of the host semiconductor, $\varepsilon_\ell^{\rm e}$ and $\varepsilon_j^{\rm h}$ stand for the energy levels of electrons and holes, respectively, with $\ell, j = 1, 2, \cdots$. In addition, ω_{em} represents the frequency of spontaneous emission from photo-excited excitons, and the ground states of electrons and holes are coupled to their first excited states by lattice phonons at finite temperatures.

For photo-excited spin-degenerated electrons in the conduction band, the semiconductor Bloch equations with $\ell = 1, 2, \cdots$ are given by

$$\frac{dn_\ell^{\rm e}}{dt} = \frac{2}{\hbar}\sum_j {\rm Im}\left[\left(Y_\ell^j\right)^*\left(\mathscr{M}_{\ell,j}^{\rm eh} - Y_\ell^j V_{\ell,j;j,\ell}^{\rm eh}\right)\right] + \left.\frac{\partial n_\ell^{\rm e}}{\partial t}\right|_{\rm rel} - \delta_{\ell,1}\mathscr{R}_{\rm sp}\, n_1^{\rm e}\, n_1^{\rm h}\,, \tag{19}$$

where $\mathscr{R}_{\rm sp}$ is the spontaneous emission rate and $n_\ell^{\rm e}$ represents the electron level population. In Eq. (19), the term marked 'rel' is the non-radiative energy relaxation for $n_\ell^{\rm e}$, and the Y_ℓ^j, $\mathscr{M}_{\ell,j}^{\rm eh}$, and $V_{\ell,j;j,\ell}^{\rm eh}$ terms are given later in the text.

Similarly, for spin-degenerate holes in the valence band, the semiconductor Bloch equations with $j = 1, 2, \cdots$ are found to be

$$\frac{dn_j^{\rm h}}{dt} = \frac{2}{\hbar}\sum_\ell {\rm Im}\left[\left(Y_\ell^j\right)^*\left(\mathscr{M}_{\ell,j}^{\rm eh} - Y_\ell^j V_{\ell,j;j,\ell}^{\rm eh}\right)\right] + \left.\frac{\partial n_j^{\rm h}}{\partial t}\right|_{\rm rel} - \delta_{j,1}\mathscr{R}_{\rm sp}\, n_1^{\rm e}\, n_1^{\rm h}\,, \tag{20}$$

where $n_j^{\rm h}$ stands for the hole energy level population. Again, the non-radiative energy relaxation for $n_j^{\rm h}$ is incorporated in Eq. (20). Moreover, we know from Eqs. (19) and (20) that

#217702 - $15.00 USD Received 23 Jul 2014; accepted 16 Sep 2014; published 30 Oct 2014

$$N_{\rm e}(t) = 2\sum_{\ell} n_{\ell}^{\rm e}(t) = 2\sum_{j} n_{j}^{\rm h}(t) = N_{\rm h}(t)\ , \tag{21}$$

where $N_{\rm e}(t)$ and $N_{\rm h}(t)$ are the total number of photo-excited electrons and holes, respectively, in the quantum dot at time t.

Finally, for spin-averaged e-h plasmas, the induced interband optical coherence, which is introduced in Eqs. (19) and (20), with $j = 1, 2, \cdots$ and $\ell = 1, 2, \cdots$ satisfies the following equations,

$$\begin{aligned} i\hbar\frac{d}{dt}Y_{\ell}^{j} = &\left[\overline{\varepsilon}_{\ell}^{\rm e}(\omega) + \overline{\varepsilon}_{j}^{\rm h}(\omega) - \hbar(\omega + i\gamma_0)\right]Y_{\ell}^{j} + \left(1 - n_{\ell}^{\rm e} - n_{j}^{\rm h}\right)\left(\mathscr{M}_{\ell,j}^{\rm eh} - Y_{\ell}^{j}V_{\ell,j;j,\ell}^{\rm eh}\right) \\ &+ Y_{\ell}^{j}\left[\sum_{j_1} n_{j_1}^{\rm h}\left(V_{j,j_1;j_1,j}^{\rm hh} - V_{j,j_1;j,j_1}^{\rm hh}\right) - \sum_{\ell_1} n_{\ell_1}^{\rm e}V_{\ell_1,j;j,\ell_1}^{\rm eh}\right] \\ &+ Y_{\ell}^{j}\left[\sum_{\ell_1} n_{\ell_1}^{\rm e}\left(V_{\ell,\ell_1;\ell_1,\ell}^{\rm ee} - V_{\ell,\ell_1;\ell,\ell_1}^{\rm ee}\right) - \sum_{j_1} n_{j_1}^{\rm h}V_{\ell,j_1;j_1,\ell}^{\rm eh}\right]\ , \end{aligned} \tag{22}$$

where $\hbar\gamma_0 = \hbar\gamma_{\rm eh} + \hbar\gamma_{ext}$ is the total energy-level broadening due to both the finite carrier lifetime and the loss of an external evanescent field, ω is the frequency of the external field, and $\overline{\varepsilon}_{\ell}^{\rm e}(\omega)$ and $\overline{\varepsilon}_{j}^{\rm h}(\omega)$ are the kinetic energies of dressed single electrons and holes, respectively (see Appendix A with $\alpha = 1$). In Eq. (22), the diagonal dephasing (γ_0) of Y_{ℓ}^{j}, the renormalization of interband Rabi coupling ($Y_{\ell}^{j}V_{\ell,j;j,\ell}^{\rm eh}$), the renormalization of electron and hole energies (third and fourth terms on the right-hand side), as well as the exciton binding energy, are all taken into consideration. Since the e-h plasmas are independent of spin index in this case, they can be excited by both left-circularly and right-circularly polarized light. The off-diagonal dephasing of Y_{ℓ}^{j} has been neglected due to low carrier density.

The steady-state solution to Eq. (22), i.e. under the condition of $dY_{\ell}^{j}/dt = 0$, is found to be

$$Y_{\ell}^{j}(t|\omega) = \left[\frac{1 - n_{\ell}^{\rm e}(t) - n_{j}^{\rm h}(t)}{\hbar(\omega + i\gamma_0) - \hbar\overline{\Omega}_{\ell,j}^{\rm eh}(\omega|t)}\right]\mathscr{M}_{\ell,j}^{\rm eh}(t)\ , \tag{23}$$

where the photon and Coulomb renormalized interband energy-level separation $\hbar\overline{\Omega}_{\ell,j}^{\rm eh}(\omega|t)$ is given by

$$\begin{aligned} \hbar\overline{\Omega}_{\ell,j}^{\rm eh}(\omega|t) = &\overline{\varepsilon}_{\ell}^{\rm e}(\omega|t) + \overline{\varepsilon}_{j}^{\rm h}(\omega|t) - V_{\ell,j;j,\ell}^{eh} + \sum_{\ell_1} n_{\ell_1}^{\rm e}(t)\left(V_{\ell,\ell_1;\ell_1,\ell}^{\rm ee} - V_{\ell,\ell_1;\ell,\ell_1}^{\rm ee}\right) \\ &+ \sum_{j_1} n_{j_1}^{\rm h}(t)\left(V_{j,j_1;j_1,j}^{\rm hh} - V_{j,j_1;j,j_1}^{\rm hh}\right) - \sum_{\ell_1\neq\ell} n_{\ell_1}^{\rm e}(t)V_{\ell_1,j;j,\ell_1}^{\rm eh} - \sum_{j_1\neq j} n_{j_1}^{\rm h}(t)V_{\ell,j_1;j_1,\ell}^{\rm eh}\ . \end{aligned} \tag{24}$$

The steady-state solution in Eq. (23) can be substituted into Eqs. (19) and (20) above.

The Coulomb interaction matrix elements introduced in Eqs.(19), (20) and (22) are defined as

$$\begin{aligned} V_{\ell_1,\ell_2;\ell_3,\ell_4}^{\rm ee} &= \int d^3\mathbf{r}\int d^3\mathbf{r}'\left[\psi_{\ell_1}^{\rm e}(\mathbf{r})\right]^{*}\left[\psi_{\ell_2}^{\rm e}(\mathbf{r}')\right]^{*}\frac{e^2}{4\pi\varepsilon_0\varepsilon_b|\mathbf{r}-\mathbf{r}'|}\psi_{\ell_3}^{\rm e}(\mathbf{r}')\,\psi_{\ell_4}^{\rm e}(\mathbf{r}) \\ &= \frac{e^2}{8\pi^2\varepsilon_0\varepsilon_b}\int d^2\mathbf{q}_{\parallel}\,\mathscr{F}_{\ell_1,\ell_4}^{\rm e}(\mathbf{q}_{\parallel})\,\mathscr{F}_{\ell_2,\ell_3}^{\rm e}(-\mathbf{q}_{\parallel})\left(\frac{1}{q_{\parallel}+q_s}\right) = \left(V_{\ell_1,\ell_2;\ell_3,\ell_4}^{\rm ee}\right)^{*}\ , \end{aligned} \tag{25}$$

#217702 - $15.00 USD Received 23 Jul 2014; accepted 16 Sep 2014; published 30 Oct 2014

$$V^{\rm hh}_{j_1,j_2;j_3,j_4} = \int d^3\mathbf{r} \int d^3\mathbf{r}' \left[\psi^{\rm h}_{j_1}(\mathbf{r})\right]^* \left[\psi^{\rm h}_{j_2}(\mathbf{r}')\right]^* \frac{e^2}{4\pi\varepsilon_0\varepsilon_b|\mathbf{r}-\mathbf{r}'|}\, \psi^{\rm h}_{j_3}(\mathbf{r}')\, \psi^{\rm h}_{j_4}(\mathbf{r})$$

$$= \frac{e^2}{8\pi^2\varepsilon_0\varepsilon_b} \int d^2\mathbf{q}_\parallel\, \mathscr{F}^{\rm h}_{j_1,j_4}(\mathbf{q}_\parallel)\, \mathscr{F}^{\rm h}_{j_2,j_3}(-\mathbf{q}_\parallel) \left(\frac{1}{q+q_s}\right) = \left(V^{\rm hh}_{j_1,j_2;j_3,j_4}\right)^* , \tag{26}$$

$$V^{\rm eh}_{\ell,j;j',\ell'} = \int d^3\mathbf{r} \int d^3\mathbf{r}' \left[\psi^{\rm e}_{\ell}(\mathbf{r})\right]^* \left[\psi^{\rm h}_{j}(\mathbf{r}')\right]^* \frac{e^2}{4\pi\varepsilon_0\varepsilon_b|\mathbf{r}-\mathbf{r}'|}\, \psi^{\rm h}_{j'}(\mathbf{r}')\, \psi^{\rm e}_{\ell'}(\mathbf{r})$$

$$= \frac{e^2}{8\pi^2\varepsilon_0\varepsilon_b} \int d^2\mathbf{q}_\parallel\, \mathscr{F}^{\rm e}_{\ell,\ell'}(\mathbf{q}_\parallel)\, \mathscr{F}^{\rm h}_{j,j'}(-\mathbf{q}_\parallel) \left(\frac{1}{q+q_s}\right) = \left(V^{\rm eh}_{\ell,j;j',\ell'}\right)^* , \tag{27}$$

where the static screening length $1/q_s$ at temperatures ($k_BT \gg E_F$) is determined from

$$q_s(t) = \frac{e^2}{4\varepsilon_0\varepsilon_b \mathscr{S}\, k_{\rm B}T} \left[N_{\rm e}(t) + N_{\rm h}(t)\right] . \tag{28}$$

Here, $\mathscr{S}$ is the cross-sectional area of a quantum dot, T is the lattice temperature, $\psi^{\rm e}_\ell(\mathbf{r})$ and $\psi^{\rm h}_j(\mathbf{r})$ are the envelope wave-functions of electrons and holes in a quantum dot (see Appendix A), and ε_b is the average dielectric constant of the host semiconductor. The two dimensionless form factors (see Appendix A) introduced in Eqs. (25)-(27) for electrons and holes due to quantum confinement by a quantum dot are defined by

$$\mathscr{F}^{\rm e}_{\ell,\ell'}(\mathbf{q}_\parallel) = e^{-q_\parallel \mathscr{L}_0} \int d^2\mathbf{r}_\parallel \left[\psi^{\rm e}_\ell(\mathbf{r}_\parallel)\right]^* {\rm e}^{i\mathbf{q}_\parallel\cdot\mathbf{r}_\parallel}\, \psi^{\rm e}_{\ell'}(\mathbf{r}_\parallel) = \left[\mathscr{F}^{\rm e}_{\ell',\ell}(-\mathbf{q}_\parallel)\right]^* , \tag{29}$$

$$\mathscr{F}^{\rm h}_{j,j'}(\mathbf{q}_\parallel) = e^{-q_\parallel \mathscr{L}_0} \int d^2\mathbf{r}_\parallel \left[\psi^{\rm h}_j(\mathbf{r}_\parallel)\right]^* {\rm e}^{i\mathbf{q}_\parallel\cdot\mathbf{r}_\parallel}\, \psi^{\rm h}_{j'}(\mathbf{r}_\parallel) = \left[\mathscr{F}^{\rm h}_{j',j}(-\mathbf{q}_\parallel)\right]^* , \tag{30}$$

where $\mathscr{L}_0$ is the thickness of a disk-like quantum dot. In addition, the matrix elements employed in Eqs. (19), (20) and (22) for the Rabi coupling between photo-excited carriers and an evanescent external field $E(\mathbf{r};t) = \theta(t)E(\mathbf{r};\omega)e^{-i\omega t}$ are given by

$$\mathscr{M}^{\rm eh}_{\ell,j}(t) = -\delta_{\ell,1}\,\delta_{j,1}\,\theta(t) \left[E^{\rm eh}_{\ell,j}(\omega)\cdot\mathbf{d}_{\rm c,v}\right] , \tag{31}$$

where $\theta(x)$ is a unit step function, the static interband dipole moment $\mathbf{d}_{\rm c,v}$ (see Appendix A) is

$$\mathbf{d}_{\rm c,v} = \int d^3\mathbf{r}\, [u_{\rm c}(\mathbf{r})]^*\, \mathbf{r}\, u_{\rm v}(\mathbf{r}) = \mathbf{d}^*_{\rm c,v} , \tag{32}$$

$u_{\rm c}(\mathbf{r})$ and $u_{\rm v}(\mathbf{r})$ are the Bloch functions associated with conduction and valence bands at the Γ-point in the first Brillouin zone of the host semiconductor, and the effective electric field coupled to the quantum dot is

$$E^{\rm eh}_{\ell,j}(\omega) = \int d^3\mathbf{r}\, [\psi^{\rm e}_\ell(\mathbf{r})]^*\, E(\mathbf{r};\omega) \left[\psi^{\rm h}_j(\mathbf{r})\right]^* . \tag{33}$$

The Boltzmann-type scattering term [33] for non-radiative electron energy relaxation in Eq. (19) is

$$\left.\frac{\partial n^{\rm e}_\ell}{\partial t}\right|_{\rm rel} = \mathscr{W}^{\rm (in)}_\ell (1-n^{\rm e}_\ell) - \mathscr{W}^{\rm (out)}_\ell\, n^{\rm e}_\ell , \tag{34}$$

where the microscopic scattering-in and scattering-out rates are calculated as

#217702 - $15.00 USD Received 23 Jul 2014; accepted 16 Sep 2014; published 30 Oct 2014

$$\mathscr{W}_{\ell}^{(\mathrm{in})} = \frac{2\pi}{\hbar}\sum_{\ell'}{}' \left|V^{\mathrm{ep}}_{\ell,\ell'}\right|^2 n^{\mathrm{e}}_{\ell'} \left\{ \mathscr{N}_{\mathrm{ph}}(\Omega_0)\left[\frac{\hbar\Gamma_{\mathrm{ph}}/\pi}{(\overline{\varepsilon}^{\mathrm{e}}_{\ell}-\overline{\varepsilon}^{\mathrm{e}}_{\ell'}-\hbar\Omega_0)^2+\hbar^2\Gamma^2_{\mathrm{ph}}}\right] \right.$$
$$\left. + \left[\mathscr{N}_{\mathrm{ph}}(\Omega_0)+1\right]\left[\frac{\hbar\Gamma_{\mathrm{ph}}/\pi}{(\overline{\varepsilon}^{\mathrm{e}}_{\ell}-\overline{\varepsilon}^{\mathrm{e}}_{\ell'}+\hbar\Omega_0)^2+\hbar^2\Gamma^2_{\mathrm{ph}}}\right]\right\}$$
$$+\frac{2\pi}{\hbar}\sum_{\ell'}{}'\sum_{j,j'}{}' \left|V^{\mathrm{eh}}_{\ell,j;j',\ell'}\right|^2 (1-n^{\mathrm{h}}_{j})\, n^{\mathrm{h}}_{j'}\, n^{\mathrm{e}}_{\ell'} \left[\frac{\hbar\gamma_{\mathrm{eh}}/\pi}{(\overline{\varepsilon}^{\mathrm{e}}_{\ell}+\overline{\varepsilon}^{\mathrm{h}}_{j}-\overline{\varepsilon}^{\mathrm{e}}_{\ell'}-\overline{\varepsilon}^{\mathrm{h}}_{j'})^2+\hbar^2\gamma^2_{\mathrm{eh}}}\right], \tag{35}$$

$$\mathscr{W}_{\ell}^{(\mathrm{out})} = \frac{2\pi}{\hbar}\sum_{\ell'}{}' \left|V^{\mathrm{ep}}_{\ell,\ell'}\right|^2 (1-n^{\mathrm{e}}_{\ell'}) \left\{ \mathscr{N}_{\mathrm{ph}}(\Omega_0)\left[\frac{\hbar\Gamma_{\mathrm{ph}}/\pi}{(\overline{\varepsilon}^{\mathrm{e}}_{\ell'}-\overline{\varepsilon}^{\mathrm{e}}_{\ell}-\hbar\Omega_0)^2+\hbar^2\Gamma^2_{\mathrm{ph}}}\right] \right.$$
$$\left. + \left[\mathscr{N}_{\mathrm{ph}}(\Omega_0)+1\right]\left[\frac{\hbar\Gamma_{\mathrm{ph}}/\pi}{(\overline{\varepsilon}^{\mathrm{e}}_{\ell'}-\overline{\varepsilon}^{\mathrm{e}}_{\ell}+\hbar\Omega_0)^2+\hbar^2\Gamma^2_{\mathrm{ph}}}\right]\right\}$$
$$+\frac{2\pi}{\hbar}\sum_{\ell'}{}'\sum_{j,j'}{}' \left|V^{\mathrm{eh}}_{\ell',j;j',\ell}\right|^2 (1-n^{\mathrm{e}}_{\ell'})\,(1-n^{\mathrm{h}}_{j})\, n^{\mathrm{h}}_{j'} \left[\frac{\hbar\gamma_{\mathrm{eh}}/\pi}{(\overline{\varepsilon}^{\mathrm{e}}_{\ell'}+\overline{\varepsilon}^{\mathrm{h}}_{j}-\overline{\varepsilon}^{\mathrm{e}}_{\ell}-\overline{\varepsilon}^{\mathrm{h}}_{j'})^2+\hbar^2\gamma^2_{\mathrm{eh}}}\right]. \tag{36}$$

Here,the primed summations in Eqs. (35) and (36) exclude the terms satisfying either $j=j'$ or $\ell'=\ell$, $\mathscr{N}_{\mathrm{ph}}(\Omega_0)=[\exp(\hbar\Omega_0/k_{\mathrm{B}}T)-1]^{-1}$ is the Bose function for the thermal-equilibrium phonons, and Ω_0 and Γ_{ph} are the frequency and lifetime of longitudinal-optical phonons in the host semiconductor. Similarly, the Boltzmann-type scattering term for hole non-radiative energy relaxation in Eq. (20) is

$$\left.\frac{\partial n^{\mathrm{h}}_{j}}{\partial t}\right|_{\mathrm{rel}} = \overline{\mathscr{W}}^{(\mathrm{in})}_{j}(1-n^{\mathrm{h}}_{j}) - \overline{\mathscr{W}}^{(\mathrm{out})}_{j}\, n^{\mathrm{h}}_{j}\,, \tag{37}$$

where the scattering-in and scattering-out rates are

$$\overline{\mathscr{W}}^{(\mathrm{in})}_{j} = \frac{2\pi}{\hbar}\sum_{j'}{}' \left|V^{\mathrm{hp}}_{j,j'}\right|^2 n^{\mathrm{h}}_{j'} \left\{ \mathscr{N}_{\mathrm{ph}}(\Omega_0)\left[\frac{\hbar\Gamma_{\mathrm{ph}}/\pi}{(\overline{\varepsilon}^{\mathrm{h}}_{j}-\overline{\varepsilon}^{\mathrm{h}}_{j'}-\hbar\Omega_0)^2+\hbar^2\Gamma^2_{\mathrm{ph}}}\right] \right.$$
$$\left. + \left[\mathscr{N}_{\mathrm{ph}}(\Omega_0)+1\right]\left[\frac{\hbar\Gamma_{\mathrm{ph}}/\pi}{(\overline{\varepsilon}^{\mathrm{h}}_{j}-\overline{\varepsilon}^{\mathrm{h}}_{j'}+\hbar\Omega_0)^2+\hbar^2\Gamma^2_{\mathrm{ph}}}\right]\right\}$$
$$+\frac{2\pi}{\hbar}\sum_{\ell,\ell'}{}'\sum_{j'}{}' \left|V^{\mathrm{eh}}_{\ell,j;j',\ell'}\right|^2 (1-n^{\mathrm{e}}_{\ell})\, n^{\mathrm{h}}_{j'}\, n^{\mathrm{e}}_{\ell'} \left[\frac{\hbar\gamma_{\mathrm{eh}}/\pi}{(\overline{\varepsilon}^{\mathrm{e}}_{\ell}+\overline{\varepsilon}^{\mathrm{h}}_{j}-\overline{\varepsilon}^{\mathrm{e}}_{\ell'}-\overline{\varepsilon}^{\mathrm{h}}_{j'})^2+\hbar^2\gamma^2_{\mathrm{eh}}}\right], \tag{38}$$

$$\overline{\mathscr{W}}^{(\mathrm{out})}_{j} = \frac{2\pi}{\hbar}\sum_{j'}{}' \left|V^{\mathrm{hp}}_{j,j'}\right|^2 (1-n^{\mathrm{h}}_{j'}) \left\{ \mathscr{N}_{\mathrm{ph}}(\Omega_0)\left[\frac{\hbar\Gamma_{\mathrm{ph}}/\pi}{(\overline{\varepsilon}^{\mathrm{h}}_{j'}-\overline{\varepsilon}^{\mathrm{h}}_{j}-\hbar\Omega_0)^2+\hbar^2\Gamma^2_{\mathrm{ph}}}\right] \right.$$
$$\left. + \left[\mathscr{N}_{\mathrm{ph}}(\Omega_0)+1\right]\left[\frac{\hbar\Gamma_{\mathrm{ph}}/\pi}{(\overline{\varepsilon}^{\mathrm{h}}_{j'}-\overline{\varepsilon}^{\mathrm{h}}_{j}+\hbar\Omega_0)^2+\hbar^2\Gamma^2_{\mathrm{ph}}}\right]\right\}$$

#217702 - $15.00 USD Received 23 Jul 2014; accepted 16 Sep 2014; published 30 Oct 2014

$$+\frac{2\pi}{\hbar}\sum_{\ell,\ell'}{}'\sum_{j'}{}'\left|V^{\rm eh}_{\ell,j';j,\ell'}\right|^2(1-n^{\rm e}_{\ell})(1-n^{\rm h}_{j'})n^{\rm e}_{\ell'}\left[\frac{\overline{\hbar\gamma}_{\rm eh}/\pi}{(\overline{\varepsilon}^{\rm e}_{\ell}+\overline{\varepsilon}^{\rm h}_{j'}-\overline{\varepsilon}^{\rm e}_{\ell'}-\overline{\varepsilon}^{\rm h}_{j})^2+\hbar^2\gamma^2_{\rm eh}}\right], \tag{39}$$

and again the primed summations in Eqs. (38) and (39) exclude the terms satisfying either $j'=j$ or $\ell=\ell'$. The coupling between the longitudinal-optical phonons and electrons or holes in Eqs. (35), (36), (38) and (39) are

$$\left|V^{\rm ep}_{\ell,\ell'}\right|^2=\frac{e^2\hbar\Omega_0}{8\pi^2\varepsilon_0}\left(\frac{1}{\varepsilon_\infty}-\frac{1}{\varepsilon_s}\right)\int d^2\mathbf{q}_\parallel\left|\mathscr{F}^{\rm e}_{\ell,\ell'}(\mathbf{q}_\parallel)\right|^2\left(\frac{1}{q_\parallel+q_s}\right), \tag{40}$$

$$\left|V^{\rm hp}_{\ell,\ell'}\right|^2=\frac{e^2\hbar\Omega_0}{8\pi^2\varepsilon_0}\left(\frac{1}{\varepsilon_\infty}-\frac{1}{\varepsilon_s}\right)\int d^2\mathbf{q}_\parallel\left|\mathscr{F}^{\rm h}_{j,j'}(\mathbf{q}_\parallel)\right|^2\left(\frac{1}{q_\parallel+q_s}\right), \tag{41}$$

where ε_∞ and ε_s are the high-frequency and static dielectric constants of the host polar semiconductor.

By generalizing the Kubo-Martin-Schwinger relation [20], the time-dependent spontaneous emission rate, $\mathscr{R}_{\rm sp}(t)$, introduced in Eqs. (19) and (20), can be expressed as

$$\mathscr{R}_{\rm sp}(t)=\frac{\left|\mathbf{d}'_{\rm c,v}(t)\right|^2}{\varepsilon_0\sqrt{\varepsilon_b}}\left|\int d^3\mathbf{r}\,\psi^{\rm e}_1(\mathbf{r})\,\psi^{\rm h}_1(\mathbf{r})\right|^2\int_0^\infty d\omega'\,\theta\left[\hbar\omega'-\mathscr{E}_{\rm c}(t)-\overline{\varepsilon}^{\rm e}_1(\omega|t)-\overline{\varepsilon}^{\rm h}_1(\omega|t)\right]$$
$$\times\hbar\omega'\,\rho_0(\omega')\left\{\frac{\overline{\hbar\gamma}_{\rm eh}}{[\hbar\omega'-\mathscr{E}_{\rm c}(t)-\overline{\varepsilon}^{\rm e}_1(\omega|t)-\overline{\varepsilon}^{\rm h}_1(\omega|t)]^2+\hbar^2\gamma^2_{\rm eh}}\right\}, \tag{42}$$

where

$$\left|\mathbf{d}'_{\rm c,v}(t)\right|^2=\frac{e^2\hbar^2}{2m_0\,\mathscr{E}_{\rm G}(T)}\left[1+\frac{\mathscr{E}_{\rm c}(t)}{\mathscr{E}_{\rm G}(T)}\right]\left(\frac{m_0}{m^*_{\rm e}}-1\right), \tag{43}$$

$\mathscr{E}_{\rm G}(T)=\mathscr{E}_{\rm G}(0)-5.41\times10^{-4}\,T^2/(T+204)$ (in units of eV) is the energy bandgap of the host semiconductor, $\rho_0(\omega)=\omega^2/c^3\pi^2\hbar$ is the density-of-states of spontaneously-emitted photons in vacuum, m_0 is the free electron mass, $m^*_{\rm e}$ is the effective mass of electrons, and the Coulomb renormalization of the energy bandgap $\mathscr{E}_{\rm c}(t)$ is found to be

$$\mathscr{E}_{\rm c}(t)=\sum_{\ell_1}n^{\rm e}_{\ell_1}(t)\left(V^{\rm ee}_{1,\ell_1;\ell_1,1}-V^{\rm ee}_{1,\ell_1;1,\ell_1}\right)+\sum_{j_1}n^{\rm h}_{j_1}(t)\left(V^{\rm hh}_{1,j_1;j_1,1}-V^{\rm hh}_{1,j_1;1,j_1}\right)$$
$$-\sum_{\ell_1}n^{\rm e}_{\ell_1}(t)V^{\rm eh}_{\ell_1,1;1,\ell_1}-\sum_{j_1}n^{\rm h}_{j_1}(t)V^{\rm eh}_{1,j_1;j_1,1}-\left[1-n^{\rm e}_1(t)-n^{\rm h}_1(t)\right]V^{\rm eh}_{1,1;1,1}\,. \tag{44}$$

In Eq. (44), the first two terms are associated with the Hartree-Fock energies of electrons and holes, while the remaining terms are related to the exciton binding energy.

Finally, the photo-induced interband optical polarization $\mathscr{P}^{\rm loc}(\mathbf{r};\omega)$, which is related to the induced interband optical coherence, by dressed electrons in the quantum dot is given by [2]

$$\mathscr{P}^{\rm loc}(\mathbf{r};\omega)=2\,|\xi(\mathbf{r})|^2\,\mathbf{d}_{\rm c,v}\left\{\int d^3\mathbf{r}'\,\psi^{\rm e}_1(\mathbf{r}')\,\psi^{\rm h}_1(\mathbf{r}')\right\}$$
$$\times\frac{1}{\hbar}\lim_{t\to\infty}\left[\frac{1-n^{\rm e}_1(t)-n^{\rm h}_1(t)}{\omega+i\gamma_0-\overline{\Omega}^{\rm eh}_{1,1}(\omega|t)}\right]\mathscr{M}^{\rm eh}_{1,1}(t)\,, \tag{45}$$

where $\mathbf{d}_{\rm c,v}=d_{\rm c,v}\,\hat{\mathbf{e}}_{\rm d}$ represents the interband dipole moment [see Eq. (32)], $\hat{\mathbf{e}}_{\rm d}$ is the unit vector of the dipole moment, and $|\xi(\mathbf{r})|^2$ comes from the confinement of a quantum dot.

#217702 - $15.00 USD Received 23 Jul 2014; accepted 16 Sep 2014; published 30 Oct 2014

2.4. Self-consistent field equation

Since the wavelength of the incident light is much larger than the size of a quantum dot, we can treat the quantum dot, which is excited resonantly by the incident light, as a point dipole at $\mathbf{r} = \mathbf{r}_0 = (0,0,z_0)$, i.e. we can assume $\mathscr{P}^{\rm loc}(\mathbf{r}';\omega) = \mathscr{P}^{\rm loc}(\omega)\,\delta(\mathbf{r}'-\mathbf{r}_0)$ in Eq. (4) to neglect its geometry effect. This greatly simplifies the calculation and gives rise to

$$E_\mu(\mathbf{r};\omega) = E_\mu^{(0)}(\mathbf{r};\omega) - \frac{\omega^2}{\varepsilon_0 c^2}\sum_\nu \mathscr{G}_{\mu\nu}(\mathbf{r},\mathbf{r}_0;\omega)\,\mathscr{P}_\nu^{\rm loc}(\omega)\,, \tag{46}$$

where

$$\mathscr{P}^{\rm loc}(\omega) = 2\mathbf{d}_{\rm c,v}\left\{\int d^3\mathbf{r}'\,\psi_1^{\rm e}(\mathbf{r}')\,\psi_1^{\rm h}(\mathbf{r}')\right\}$$

$$\times\frac{1}{\hbar}\lim_{t\to\infty}\left\{\frac{1-n_1^{\rm e}(t)-n_1^{\rm h}(t)}{\omega+i\gamma_0-\overline{\Omega}_{1,1}^{\rm eh}(\omega|t)}\right\}\mathscr{M}_{1,1}^{\rm eh}(t)\,, \tag{47}$$

$$\mathscr{M}_{1,1}^{\rm eh}(t) = -\theta(t)\,[E(\mathbf{r}_0;\omega)\cdot\mathbf{d}_{\rm c,v}]\left\{\int d^3\mathbf{r}\,\psi_1^{\rm e}(\mathbf{r})\,\psi_1^{\rm h}(\mathbf{r})\right\}^*\,. \tag{48}$$

Substituting Eqs. (47) and (48) into Eq. (46), we get the following nonlinear equations for the electromagnetic field

$$E_\mu(\mathbf{r};\omega) = E_\mu^{(0)}(\mathbf{r};\omega) + \frac{2\omega^2}{\varepsilon_0 c^2}\,[E(\mathbf{r}_0;\omega)\cdot\mathbf{d}_{\rm c,v}]\,d_{\rm c,v}\left|\int d^3\mathbf{r}'\,\psi_1^{\rm e}(\mathbf{r}')\,\psi_1^{\rm h}(\mathbf{r}')\right|^2$$

$$\times\frac{1}{\hbar}\lim_{t\to\infty}\left\{\frac{1-n_1^{\rm e}(t)-n_1^{\rm h}(t)}{\omega+i\gamma_0-\overline{\Omega}_{1,1}^{\rm eh}(\omega|t)}\right\}\sum_\nu \mathscr{G}_{\mu\nu}(\mathbf{r},\mathbf{r}_0;\omega)\,\hat{e}_{\rm d}^\nu\,, \tag{49}$$

where the quantum-dot level populations $n_\ell^{\rm e}(t)$ and $n_j^{\rm h}(t)$ depend nonlinearly on $E(\mathbf{r}_0;\omega)$ in the strong-coupling regime.

If the electromagnetic field is not very strong, we can neglect the pumping effect. In this linear-response regime, we can write down the electron and hole populations in a thermal-equilibrium state [without solving Eqs. (19) and (20)]

$$n_\ell^{\rm e}(t) \approx f_0(\overline{\varepsilon}_\ell^{\rm e}) \equiv \frac{1}{\exp[(\overline{\varepsilon}_\ell^{\rm e}-\mu_{\rm e})/k_BT]+1}\,, \tag{50}$$

$$n_j^{\rm h}(t) \approx f_0(\overline{\varepsilon}_j^{\rm h}) \equiv \frac{1}{\exp[(\overline{\varepsilon}_j^{\rm h}-\mu_{\rm h})/k_BT]+1}\,, \tag{51}$$

where $f_0(x)$ is the Fermi function, and $\mu_{\rm e}$ and $\mu_{\rm h}$ are the chemical potentials of electrons and holes, respectively, determined by Eq. (21). As a result of Eqs. (50) and (51), we get from Eq. (49) the *linearized* self-consistent field equation at $\mathbf{r} = \mathbf{r}_0$

$$\sum_\nu \mathscr{A}_{\mu\nu}(\mathbf{r}_0;\omega)\,E_\nu(\mathbf{r}_0;\omega) = E_\mu^{(0)}(\mathbf{r}_0;\omega) \tag{52}$$

with

$$\mathscr{A}_{\mu\nu}(\mathbf{r}_0;\omega) = \delta_{\mu\nu} - \frac{2\omega^2}{\varepsilon_0 c^2\hbar}\left[\frac{1-f_0(\overline{\varepsilon}_1^{\rm e})-f_0(\overline{\varepsilon}_1^{\rm h})}{\omega+i\gamma_0-\overline{\Omega}_{1,1}^{\rm eh}(\omega)}\right]\left|\int d^3\mathbf{r}'\,\psi_1^{\rm e}(\mathbf{r}')\,\psi_1^{\rm h}(\mathbf{r}')\right|^2$$

#217702 - $15.00 USD Received 23 Jul 2014; accepted 16 Sep 2014; published 30 Oct 2014

$$\times d_{\mathrm{c,v}}^2 \left[\hat{e}_{\mathrm{d}}^{\nu} \sum_{\nu_1} \mathscr{G}_{\mu\nu_1}(\mathbf{r}_0, \mathbf{r}_0; \omega)\, \hat{e}_{\mathrm{d}}^{\nu_1} \right] , \tag{53}$$

where, according to Eq. (6), we have

$$\mathscr{G}_{\mu\nu}(\mathbf{r}_0, \mathbf{r}_0; \omega) = \int \frac{d^2\mathbf{k}_{\parallel}}{(2\pi)^2}\, g_{\mu\nu}(\mathbf{k}_{\parallel}, \omega | z_0, z_0) . \tag{54}$$

The solution $E(\mathbf{r}_0; \omega)$ of the linear-matrix equation in Eq. (52) can be substituted into Eq. (49) to yield the spatial distribution of the electromagnetic field $E(\mathbf{r}; \omega)$ at all positions other than $\mathbf{r} = \mathbf{r}_0$, i.e.,

$$E_{\mu}(\mathbf{r}; \omega) = E_{\mu}^{(0)}(\mathbf{r}; \omega) + \frac{2\omega^2}{\varepsilon_0 c^2 \hbar} \left[\sum_{\nu,\nu'} \hat{e}_{\mathrm{d}}^{\nu}\, \mathscr{A}_{\nu\nu'}^{-1}(\mathbf{r}_0; \omega) E_{\nu'}^{(0)}(\mathbf{r}_0; \omega) \right]$$

$$\times \left| \int d^3\mathbf{r}'\, \psi_1^{\mathrm{e}}(\mathbf{r}')\, \psi_1^{\mathrm{h}}(\mathbf{r}') \right|^2 d_{\mathrm{c,v}}^2 \left[\frac{1 - f_0(\overline{\varepsilon}_1^{\mathrm{e}}) - f_0(\overline{\varepsilon}_1^{\mathrm{h}})}{\omega + i\gamma_0 - \overline{\Omega}_{1,1}^{\mathrm{eh}}(\omega)} \right] \sum_{\nu_1} \mathscr{G}_{\mu\nu_1}(\mathbf{r}, \mathbf{r}_0; \omega)\, \hat{e}_{\mathrm{d}}^{\nu_1} . \tag{55}$$

In order to find the coupled e-h plasma and plasmon dispersion relation $\omega = \Omega_{\mathrm{ex-pl}}(\mathbf{k}_{\parallel})$, we Fourier transform both $E(\mathbf{r}; \omega)$ and $E^{(0)}(\mathbf{r}; \omega)$ in Eq. (46) with respect to $\mathbf{r}_{\parallel}$. This leads to

$$E_{\mu}(\mathbf{k}_{\parallel}, \omega | x_3) = E_{\mu}^{(0)}(\mathbf{k}_{\parallel}, \omega | x_3) - \frac{\omega^2}{\varepsilon_0 c^2} \sum_{\nu} g_{\mu\nu}(\mathbf{k}_{\parallel}, \omega | x_3, z_0)\, \mathscr{P}_{\nu}^{\mathrm{loc}}(\omega) . \tag{56}$$

After setting $x_3 = z_0$ in Eq. (56), we get

$$\sum_{\nu} \left\{ \delta_{\mu\nu} - \frac{2\omega^2}{\varepsilon_0 c^2 \hbar} \left[\frac{1 - f_0(\overline{\varepsilon}_1^{\mathrm{e}}) - f_0(\overline{\varepsilon}_1^{\mathrm{h}})}{\omega + i\gamma_0 - \overline{\Omega}_{1,1}^{\mathrm{eh}}(\omega)} \right] \left| \int d^3\mathbf{r}'\, \psi_1^{\mathrm{e}}(\mathbf{r}')\, \psi_1^{\mathrm{h}}(\mathbf{r}') \right|^2 d_{\mathrm{c,v}}^2 \right.$$

$$\times \left. \left[\hat{e}_{\mathrm{d}}^{\nu} \sum_{\nu_1} g_{\mu\nu_1}(\mathbf{k}_{\parallel}, \omega | z_0, z_0)\, \hat{e}_{\mathrm{d}}^{\nu_1} \right] \right\} E_{\nu}(\mathbf{k}_{\parallel}, \omega | z_0) = E_{\mu}^{(0)}(\mathbf{k}_{\parallel}, \omega | z_0) . \tag{57}$$

Here, the vanishing of the determinant of the coefficient matrix in Eq. (57) determines the coupled e-h plasma and plasmon dispersion relation $\omega = \Omega_{\mathrm{ex-pl}}(\mathbf{k}_{\parallel})$. We emphasize that the assumption of thermal-equilibrium states for electrons and holes is just for obtaining analytical expressions. Therefore, some qualitative conclusions can be drawn for guidance from these analytical solutions. Our numerical results, however, are based on the non-thermal-equilibrium steady states calculated after solving self-consistently the coupled Maxwell-Bloch equations.

By assuming an incident SPP field within the x_1x_2-plane, we can write

$$E^{(0)}(\mathbf{r}; \omega_{\mathrm{sp}}) = E_{\mathrm{sp}}\, e^{i\mathbf{k}_0(\omega_{\mathrm{sp}})\cdot\mathbf{D}_0}\, \frac{c}{\omega_{\mathrm{sp}}} \left[i\hat{\mathbf{k}}_0 \beta_3(k_0, \omega_{\mathrm{sp}}) - \hat{\mathbf{x}}_3 k_0(\omega_{\mathrm{sp}}) \right] e^{i\mathbf{k}_0(\omega_{\mathrm{sp}})\cdot\mathbf{x}_{\parallel}}\, e^{-\beta_3(k_0, \omega_{\mathrm{sp}})x_3} , \tag{58}$$

where $\mathbf{x}_{\parallel} = \{x_1, x_2\}$, $\hat{\mathbf{k}}_0$ and $\hat{\mathbf{x}}_3$ are the unit vectors in the $\mathbf{k}_0 = k_0(\omega_{\mathrm{sp}})\{\cos\theta_0, \sin\theta_0\}$ and x_3 directions, E_{sp} is the field amplitude, ω_{sp} is the field frequency, θ_0 is the angle of the incident SPP field with respect to the x_1 direction, $\mathbf{D}_0 = \{-x_g, -y_g\}$ is the position vector of the surface grating, and the two wave numbers are

$$k_0(\omega_{\mathrm{sp}}) = \frac{\omega_{\mathrm{sp}}}{c} \sqrt{\frac{\varepsilon_{\mathrm{d}}\, \varepsilon_{\mathrm{M}}(\omega_{\mathrm{sp}})}{\varepsilon_{\mathrm{d}} + \varepsilon_{\mathrm{M}}(\omega_{\mathrm{sp}})}} , \tag{59}$$

#217702 - $15.00 USD Received 23 Jul 2014; accepted 16 Sep 2014; published 30 Oct 2014

$$\beta_3(k_0,\omega_{\rm sp})=\sqrt{k_0^2(\omega_{\rm sp})-\frac{\omega_{\rm sp}^2}{c^2}}\,, \tag{60}$$

with $\mathrm{Re}[k_0(\omega_{\rm sp})]\geq 0$ and $\mathrm{Re}[\beta_3(k_0,\omega_{\rm sp})]\geq 0$. Here, the in-plane wave number k_0 is produced by the surface-grating diffraction of the *p*-polarized normally-incident light, which in turn determines the resonant frequency ω of the SPP mode. Equation (59) stands for the full dispersion relation of the SPP field, including both radiative and non-radiative parts. From Eq. (58), it is easy to find its Fourier transformed expression

$$E^{(0)}(\mathbf{k}_{\|},\omega_{\rm sp}|z_0)=\delta(\mathbf{k}_{\|}-\mathbf{k}_0)\,E_{\rm sp}\,e^{i\mathbf{k}_0(\omega_{\rm sp})\cdot\mathbf{D}_0}\,\frac{(2\pi)^2 c}{\omega_{\rm sp}}$$
$$\times\left[i\hat{\mathbf{k}}_0\beta_3(k_0,\omega_{\rm sp})-\hat{\mathbf{x}}_3 k_0(\omega_{\rm sp})\right]\,e^{-\beta_3(k_0,\omega_{\rm sp})z_0}\,. \tag{61}$$

2.5. Quantum-dot absorption

On the basis of the electromagnetic field $E(\mathbf{r}_0;\omega)$ at the quantum dot, we are able to compute the time-resolved nonlinear interband absorption coefficient of *dressed* electrons in a quantum dot for the SPP field [34]. In this case, we find

$$\beta_0(\omega;t)=\frac{\omega\sqrt{\varepsilon_b}}{n_{\rm spp}(\omega;t)\,c}\left[\frac{1}{\exp(\hbar\omega/k_{\rm B}T)-1}+1\right]\mathrm{Im}\left[\alpha_{\rm spp}(\omega;t)\right]\,, \tag{62}$$

where $\alpha_{\rm spp}(\omega;t)$ is the complex Lorentz function given by

$$\mathrm{Im}[\alpha_{\rm spp}(\omega;t)]=\theta(t)\left(\frac{2}{\varepsilon_0\varepsilon_b\mathscr{V}|E^{(0)}(\mathbf{r}_0;\omega)|^2}\right)|E(\mathbf{r}_0;\omega)\cdot\mathbf{d}_{\rm c,v}|^2\left|\int d^3\mathbf{r}\,\psi_1^{\rm e}(\mathbf{r})\,\psi_1^{\rm h}(\mathbf{r})\right|^2$$
$$\times\left[1-n_1^{\rm e}(t)-n_1^{\rm h}(t)\right]\left\{\frac{[A^2(\omega;t)-B^2(t)]^2+4\hbar^2\gamma_0^2A^2(\omega;t)}{[A^2(\omega;t)+B^2(t)]^2+4\hbar^2\gamma_0^2A^2(\omega;t)}\right\}\left[\frac{\hbar\gamma_0}{\Delta^2(\omega;t)+\hbar^2\gamma_0^2}\right]\,, \tag{63}$$

$$\mathrm{Re}[\alpha_{\rm spp}(\omega;t)]=-\theta(t)\left(\frac{2}{\varepsilon_0\varepsilon_b\mathscr{V}|E^{(0)}(\mathbf{r}_0;\omega)|^2}\right)|E(\mathbf{r}_0;\omega)\cdot\mathbf{d}_{\rm c,v}|^2\left|\int d^3\mathbf{r}\,\psi_1^{\rm e}(\mathbf{r})\,\psi_1^{\rm h}(\mathbf{r})\right|^2$$
$$\times\left[1-n_1^{\rm e}(t)-n_1^{\rm h}(t)\right]\left\{\frac{A^4(\omega;t)-B^4(t)]^2}{[A^2(\omega;t)+B^2(t)]^2}\right\}\left[\frac{\Delta(\omega;t)}{\Delta^2(\omega;t)+\hbar^2\gamma_0^2}\right]\,, \tag{64}$$

and the scaled refractive index function $n_{\rm spp}(\omega;t)$ can be calculated by

$$n_{\rm spp}(\omega;t)=\frac{1}{\sqrt{2}}\left(1+\mathrm{Re}\left[\alpha_{\rm spp}(\omega;t)\right]\right.$$
$$\left.+\sqrt{\left\{1+\mathrm{Re}\left[\alpha_{\rm spp}(\omega;t)\right]\right\}^2+\left\{\mathrm{Im}\left[\alpha_{\rm spp}(\omega;t)\right]\right\}^2}\right)^{1/2}\,. \tag{65}$$

In Eqs. (63) and (64), the dressed-state effects on both the level population and dipole moment have been included. In addition, we have introduced the following notations in Eqs. (63) and (64)

$$\Delta(\omega;t)=\sqrt{[\mathscr{E}_{\rm G}(T)+\varepsilon_1^{\rm e}+\varepsilon_1^{\rm h}-\hbar\omega]^2+4|\mathscr{M}_{1,1}^{\rm eh}(t)|^2}\,, \tag{66}$$

$$A^2(\omega;t)=\left[\hbar\omega-\mathscr{E}_{\rm G}(T)-\varepsilon_1^{\rm e}-\varepsilon_1^{\rm h}+\Delta(\omega;t)\right]^2\,,\quad B^2(t)=4|\mathscr{M}_{1,1}^{\rm eh}(t)|^2\,. \tag{67}$$

#217702 - $15.00 USD Received 23 Jul 2014; accepted 16 Sep 2014; published 30 Oct 2014

2.6. Probing quantum-dot dressed states

We are also able to compute the time-resolved linear interband absorption coefficient of electrons, dressed by the SPP field, for a weak probe field (not the strong SPP field) on the basis of the electromagnetic field $E(\mathbf{r}_0;\omega)$ at the quantum dot calculated above [34]. Assuming a spatially-uniform probe field $E_p(t)=\theta(t-\tau)E_p e^{-i\omega_p t}$ where τ is the delay time, the probe-field absorption coefficient $\beta_{\rm abs}(\omega_p;t)$ of the lowest dressed state is given by Eq. (62) with the replacements of ω, $n_{\rm spp}$, and $\alpha_{\rm spp}$ by ω_p, $n_{\rm pf}$, and $\alpha_{\rm pf}$, respectively, where

$$\alpha_{\rm pf}(\omega_p;t)=-\theta(t-\tau)\left(\frac{2}{\varepsilon_0\varepsilon_b\mathscr{V}|E_p|^2\hbar}\right)|E_p\cdot\mathbf{d}_{\rm c,v}|^2\left|\int d^3\mathbf{r}\,\psi_1^{\rm e}(\mathbf{r})\,\psi_1^{\rm h}(\mathbf{r})\right|^2\left[1-n_1^{\rm e}(t)-n_1^{\rm h}(t)\right]$$
$$\times\left\{\frac{A^2(\omega;t)-B^2(t)}{[A^2(\omega;t)+B^2(t)]^2}\right\}\left\{\frac{A^2(\omega;t)}{\omega_p+i\gamma_{\rm eh}-\overline{\Omega}_{1,1}^{\rm eh}(\omega_-|t)}-\frac{B^2(t)}{\omega_p+i\gamma_{\rm eh}-\overline{\Omega}_{1,1}^{\rm eh}(\omega_+|t)}\right\}, \qquad (68)$$

$$n_{\rm pf}(\omega_p;t)=$$
$$\frac{1}{\sqrt{2}}\left(1+{\rm Re}\left[\alpha_{\rm pf}(\omega_p;t)\right]+\sqrt{\left\{1+{\rm Re}\left[\alpha_{\rm pf}(\omega_p;t)\right]\right\}^2+\left\{{\rm Im}\left[\alpha_{\rm pf}(\omega_p;t)\right]\right\}^2}\right)^{1/2} \qquad (69)$$

Here, using Eq. (24) we have

$$\hbar\overline{\Omega}_{1,1}^{\rm eh}(\omega_\pm|t)=\hbar\omega_\pm(t)-\left[1-n_1^{\rm e}(t)-n_1^{\rm h}(t)\right]V_{1,1;1,1}^{\rm eh}+\sum_{\ell_1}n_{\ell_1}^{\rm e}(t)\left(V_{1,\ell_1;\ell_1,1}^{\rm ee}-V_{1,\ell_1;1,\ell_1}^{\rm ee}\right)$$
$$+\sum_{j_1}n_{j_1}^{\rm h}(t)\left(V_{1,j_1;j_1,1}^{\rm hh}-V_{1,j_1;1,j_1}^{\rm hh}\right)-\sum_{\ell_1}n_{\ell_1}^{\rm e}(t)V_{\ell_1,1;1,\ell_1}^{\rm eh}-\sum_{j_1}n_{j_1}^{\rm h}(t)V_{1,j_1;j_1,1}^{\rm eh}\,, \qquad (70)$$

and

$$\hbar\omega_\pm(t)=\hbar\omega\pm\Delta(\omega;t)\,. \qquad (71)$$

Moreover, the time-resolved photoluminescence spectrum $\mathscr{P}_{\rm em}(\omega';t)$ of dressed electrons in the quantum dot is proportional to

$$\mathscr{P}_{\rm em}(\omega';t)\propto\frac{|\mathbf{d}'_{\rm c,v}|^2}{\varepsilon_0\sqrt{\varepsilon_b}\mathscr{L}_0}n_1^{\rm e}(t)\,n_1^{\rm h}(t)\,\hbar\gamma_{\rm eh}\left\{\frac{1}{[A^2(\omega;t)+B^2(t)]^2}\right\}\left|\int d^3\mathbf{r}\,\psi_1^{\rm e}(\mathbf{r})\,\psi_1^{\rm h}(\mathbf{r})\right|^2\hbar\omega'\,\rho_0(\omega')$$
$$\times\left\{\frac{A^2(\omega;t)\,B^2(t)}{[\hbar\omega'-\mathscr{E}_{\rm c}(t)-\hbar\omega_-(t)]^2+\hbar^2\gamma_{\rm eh}^2}+\frac{A^2(\omega;t)\,B^2(t)}{[\hbar\omega'-\mathscr{E}_{\rm c}(t)-\hbar\omega_+(t)]^2+\hbar^2\gamma_{\rm eh}^2}\right.$$
$$\left.+\frac{A^4(\omega;t)+B^4(t)}{[\hbar\omega'-\mathscr{E}_{\rm c}(t)-\hbar\omega]^2+\hbar^2\gamma_{\rm eh}^2}\right\}. \qquad (72)$$

3. Numerical results and discussions

3.1. Results for the dynamics of an SPP field

In the first part of our numerical calculations, we have taken: $\mathscr{L}_0=100$ Å, $L_y=100$ Å, $m_{\rm e}^*=0.067\,m_0$, $m_{\rm h}^*=0.62\,m_0$, $\theta_0=45^{\rm o}$, $x_g=y_g=610$ Å, $\varepsilon_b=12$, $\varepsilon_s=11$, $\varepsilon_\infty=13$, $\hbar\Omega_0=36$ meV and $\hbar\gamma_{\rm eh}=\hbar\Gamma_{\rm ph}=\hbar\gamma_0$. The silver plasma frequency is 13.8×10^{15} Hz and the silver plasma dephasing is 0.1075×10^{15} Hz. The energy gap $E_{\rm G}$ of the quantum-dot host material is 1.927 eV

#217702 - $15.00 USD Received 23 Jul 2014; accepted 16 Sep 2014; published 30 Oct 2014

at $T = 300$ K. Other parameters, including T, $E_{\rm sp}$, L_x, $\hbar\gamma_0$, z_0 and $\varepsilon_{\rm d}$, will be directly indicated in the figures.

Figure 3 presents the quantum dot absorption coefficient $\beta_0(\omega_{\rm sp})$ for an SPP field, the scattered field $|\mathbf{E}_{\rm tot} - \mathbf{E}_{\rm sp}|$ of the SPP field, and the energy-level occupations for electrons $n_{\ell,e}$ and holes $n_{j,h}$ with $\ell,\ j = 1, 2$ as functions of frequency detuning $\Delta\hbar\omega_{\rm sp} \equiv \hbar\omega_{\rm sp} - (E_{\rm G} + \varepsilon_{1,e} + \varepsilon_{1,h})$. A dip is observed at resonance $\Delta\hbar\omega_{\rm sp} = 0$ in the upper-left panel, which appears to become deeper with decreasing amplitude $E_{\rm sp}$ of the SPP field in the strong-coupling regime due to a decrease in the saturated absorption. However, this dip completely disappears when $E_{\rm sp}$ drops to 25 kV/cm in the weak-coupling regime due to the suppression of the photon-dressing effect, which is accompanied by an order of magnitude increase in the absorption-peak strength. The dip in the upper-left panel corresponds to a peak in the scattered field, as can be seen from the upper-right panel of the figure. The scattered field increases with frequency detuning away from resonance, corresponding to the decreasing absorption. As a result, a minimum appears on each side of the resonance in the scattered field in the strong-coupling regime. The Maxwell-Bloch equations couple the field dynamics outside of a quantum dot with the electron dynamics inside the dot. At $E_{\rm sp} = 125$ kV/cm in the lower-right panel, we find peaks in the energy-level occupations at resonance, which are broadened by the finite carrier lifetime as well as the optical power of the SPP field. Moreover, jumps in the energy-level occupations can be seen at resonance due to Rabi splitting of the energy levels in the dressed electron states. The effect of resonant phonon absorption also plays a significant role in the finite value of $n_{2,e}$ with energy-level separations $\varepsilon_{2,e} - \varepsilon_{1,e} \approx \hbar\Omega_0$. However, as $E_{\rm sp}$ decreases to 25 kV/cm in the lower-left panel, peaks in the energy-level occupations are greatly sharpened and negatively shifted due to the suppression of the broadening from the optical power and the excitonic effect, respectively. Additionally, jumps in the energy-level occupations become invisible because the Rabi-split energy gap in this case is much smaller than the energy-level broadening from the finite lifetime of electrons (i.e. severely damped Rabi oscillations between the first electron and hole levels).

We know that a decrease in temperature T gives rise to an increase in the crystal bandgap $E_{\rm G}$. On the other hand, the localization of an SPP field (i.e. an exponential decay of the field strength on either side of a metallic surface) is greatly enhanced when the SPP frequency $\omega_{\rm sp}$ approaches that of a surface plasmon. As a result, the field at the quantum dot is expected to decrease as T is reduced. This gives rise to a higher absorption coefficient for a lower temperature, as shown in the upper-left panel of Fig. 4. Interestingly, although the suppressed absorption coefficient can be seen from $\beta_0(\omega_{\rm sp})$ for high SPP-field amplitudes, as shown by Eq. (63), from the upper-right panel of this figure we find the resonant peak at $\hbar\omega_{\rm sp} = E_{\rm G} + \varepsilon_{1,\rm e} + \varepsilon_{1,\rm h}$ initially increases with T but then decreases with T at room temperature. This subtle difference demonstrates the effect of reduced phonon absorption at $T = 77$ K on the resonant scattered field by the factor $1 - n_{\rm e}(t) - n_{\rm h}(t)$ in Eq. (49). Moreover, the strong effect of the suppressed optical-phonon absorption between two electron energy levels at 77 K is clearly demonstrated in the lower panels of Fig. 4, where the level occupation $n_{2,\rm e}$ becomes negligible at $T = 77$ K in comparison with that at $T = 300$ K.

The electron thermal dynamics due to phonon absorption has been demonstrated in Fig. 4 for various temperatures. In Fig. 5, we present the electron dynamics resulting from the optical dephasing, due to the finite lifetime of electrons, at different energy-level broadenings $\hbar\gamma_0$. As $\hbar\gamma_0$ is increased from 3 meV to 7 meV, the dip in $\beta_0(\omega_{\rm sp})$ at resonance is suppressed, leading to a single peak with a reduced strength and an increased width, as shown in the upper-left panel of the figure. This increase in the resonant absorption is further accompanied by an enhanced resonant peak for the scattered field in the upper-right panel of this figure. As expected, the energy-level occupations at $\hbar\gamma_0 = 7$ meV become much broader than those at $\hbar\gamma_0 = 3$ meV, as displayed in the lower two panels of the figure.

#217702 - $15.00 USD Received 23 Jul 2014; accepted 16 Sep 2014; published 30 Oct 2014

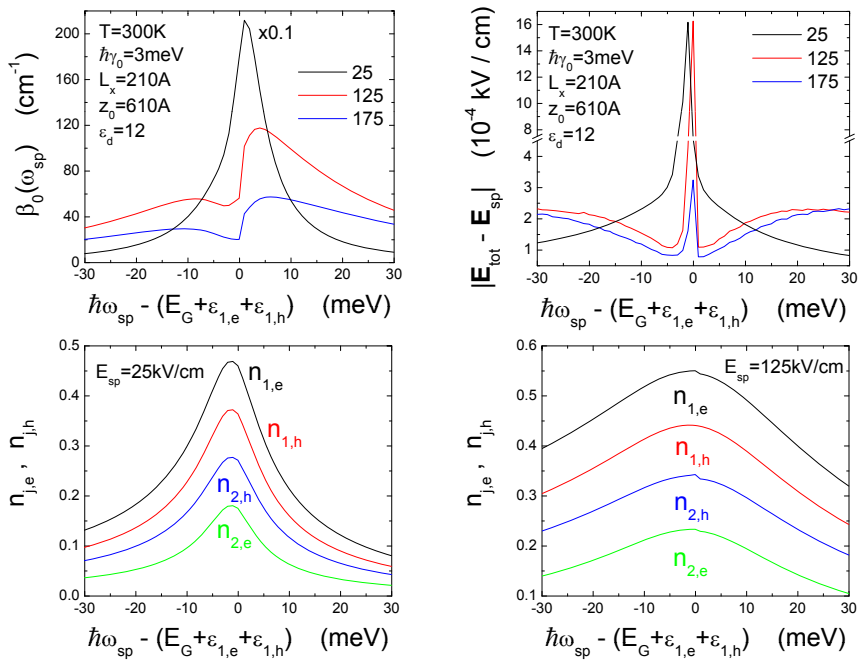

Fig. 3. Optical absorption coefficients $\beta_0(\omega_{\rm sp})$ (upper-left panel) and scattering field $|\mathbf{E}_{\rm tot}-\mathbf{E}_{\rm sp}|$ at the quantum dot (upper-right panel), as well as the energy-level occupations for electrons $n_{\ell,e}$ and holes $n_{j,h}$ (lower panels) with $\ell,\, j=1,2$, as functions of the frequency detuning $\Delta\hbar\omega_{\rm sp}\equiv\hbar\omega_{\rm sp}-(E_{\rm G}+\varepsilon_{1,e}+\varepsilon_{1,h})$. Here, the results for various amplitudes $E_{\rm sp}$ of an SPP field with frequency $\omega_{\rm sp}$ are presented in the upper panels, along with a comparison of the energy-level occupations for $E_{\rm sp}=25$ and 125 kV/cm in the lower panels. The label $\times 0.1$ in the upper-left panel indicates that the result is multiplied by a factor of 0.1.

We further notice that the effective bandgap $E_{\rm G}+\varepsilon_{1,\rm e}+\varepsilon_{1,\rm h}$ also depends on the size L_x of a quantum dot due to the quantization effect, and the effective bandgap will increase with decreasing L_x. The size effect from such an L_x dependence is displayed in Fig. 6. From the upper-left panel of Fig. 6, we find that the peak of $\beta_0(\omega_{\rm sp})$ is enhanced as L_x is reduced. This phenomenon is connected to the increased localization of the SPP field at $L_x=170$ Å as the SPP frequency approaches the saturation part of its dispersion. Moreover, the dip in $\beta_0(\omega_{\rm sp})$ is lifted somewhat uniformly at the same time due to a decreased $n_1^{\rm e}(t)$ from the enhanced Coulomb and phonon scattering at $L_x=170$ Å. Here, $\beta_0(\omega_{\rm sp})$ is proportional to the population factor $1-n_1^{\rm e}(t)-n_1^{\rm h}(t)$, as can be seen from Eq. (63). Besides the slightly-reduced resonant peak strength of the scattered field for $L_x=170$ Å (also resulting from the enhanced carrier scattering), $|\mathbf{E}_{\rm tot}-\mathbf{E}_{\rm sp}|$ keeps the same peak position, as shown in the upper-right panel of the figure. In this case, $|\mathbf{E}_{\rm tot}-\mathbf{E}_{\rm sp}|$ at the dot approaches a nonzero value at resonance, as can be seen from Eq. (55), and tends to zero rapidly away from resonance. Additionally, $n_{2,\rm h}$ is reduced for $L_x=170$ Å, as can be found from a comparison between the two lower panels of the figure. This is attributed to the reduced phonon absorption between two hole energy levels.

In Figs. 4 and 6, we vary the localization of an SPP field by changing the effective bandgap. Since the frequency of the surface plasmon (saturated dispersion part) is proportional to the factor of $1/\sqrt{1+\varepsilon_{\rm d}}$, a smaller value of $\varepsilon_{\rm d}$ implies a higher surface-plasmon frequency or a reduced localization of the SPP field. We verify the change in the SPP localization by observing the upper two panels of Fig. 7, where the absorption peak, as well as the resonant scattered-field

#217702 - $15.00 USD Received 23 Jul 2014; accepted 16 Sep 2014; published 30 Oct 2014

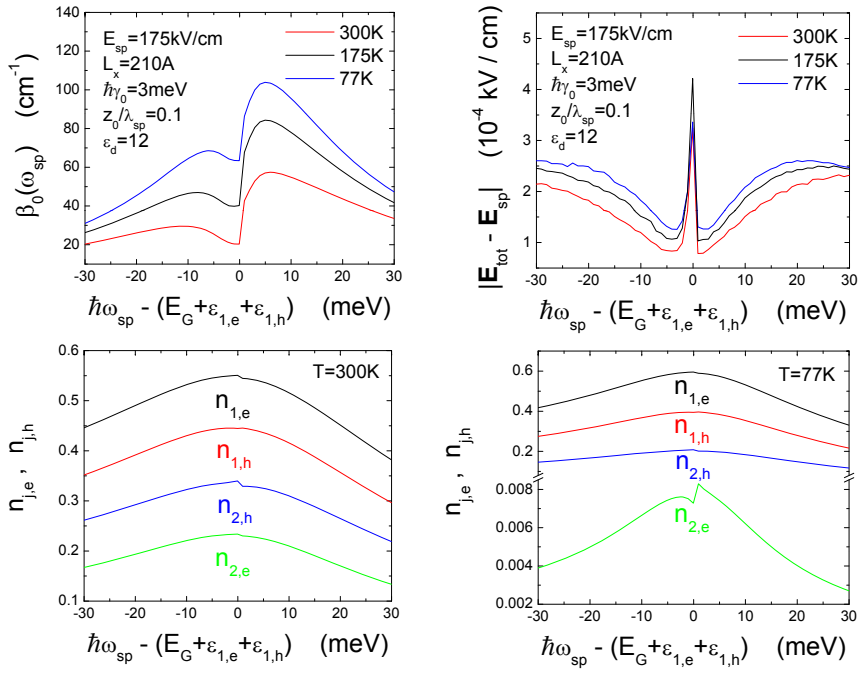

Fig. 4. $\beta_0(\omega_{\rm sp})$ (upper-left panel) and $|\mathbf{E}_{\rm tot}-\mathbf{E}_{\rm sp}|$ (upper-right panel), as well as $n_{\ell,e}$ and holes $n_{j,h}$ (lower panels), as functions of $\Delta\hbar\omega_{\rm sp}$. Here, the results for three different temperatures $T = 300$, 175 and 77 K are displayed in the upper panels, along with a comparison of $n_{\ell,e}$ and holes $n_{j,h}$ for $T = 300$ and 77 K in the lower panels.

peak, become much stronger as $\varepsilon_{\rm d}$ is increased from 8 to 12 due to the reduction of saturated absorption for a lower field strength at the quantum dot. Furthermore, from the two lower panels of this figure we also observe, via the jumps in the population curves, an enhanced Rabi-split energy gap in the electron dressed states as $\varepsilon_{\rm d}$ is reduced from 12 to 10 due to the enhanced field strength at the quantum dot.

In the presence of the localization of an SPP field, we can move a quantum dot closer to a metallic surface to gain a higher field at the quantum dot. The upper-left panel of Fig. 8 has elucidated this fact, in which a larger z_0 corresponds to a weaker field, and then, a higher absorption peak due to the reduction of saturated absorption. This fact is also reflected in the upper-right panel of the figure, where a higher resonant scattered-field peak occurs for a larger value of z_0. At $z_0 = 510$ Å, a Rabi-split energy gap at resonance is clearly visible from the lower-left-panel of the figure for electron dressed states. Additionally, at $z_0 = 710$ Å, by entering into a weak-coupling regime for a weaker field at the dot, we find sharpened resonant peaks in the energy-level occupations of electrons and holes, similar to the observation from the lower-left panel of Fig. 3.

3.2. Results for the dressed states of electrons

In the second part of the numerical calculations, besides the parameters given in the first subsection, we have fixed $L_x = 210$ Å, $\hbar\gamma_0 = 3$ meV, $z_0 = 610$ Å and $\varepsilon_{\rm d} = 12$. Other parameters, including T, $E_{\rm sp}$ and $\Delta\hbar\omega_{\rm sp}$, will be directly indicated in the figures. Additionally, $\Delta\hbar\omega_{\rm sp}$ is given with respect to the energy gap at $T = 300$ K.

From the left panel of Fig. 9 we find a strong absorption (positive) peak and a weak gain (neg-

#217702 - $15.00 USD Received 23 Jul 2014; accepted 16 Sep 2014; published 30 Oct 2014

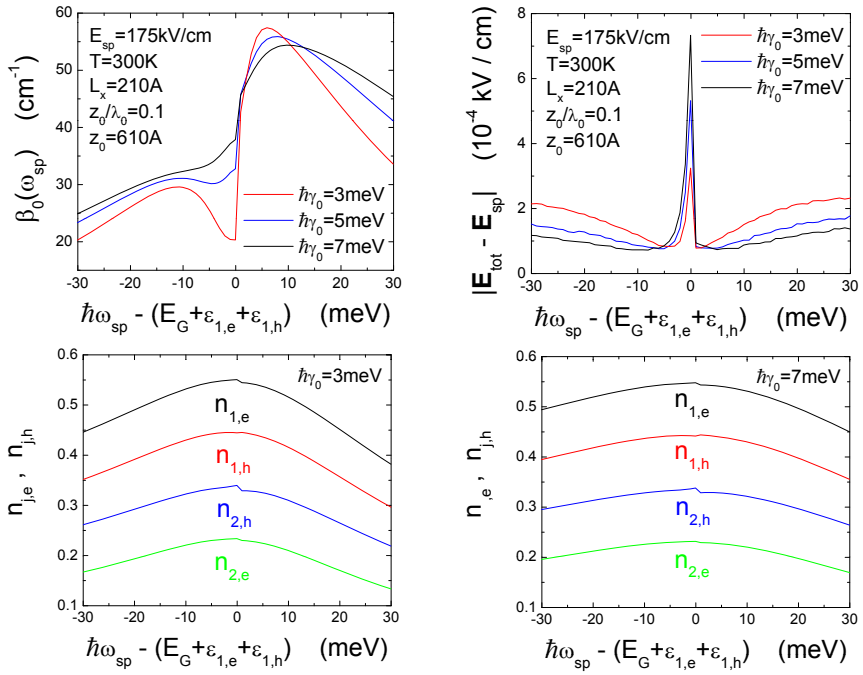

Fig. 5. $\beta_0(\omega_{\rm sp})$ (upper-left panel) and $|\mathbf{E}_{\rm tot}-\mathbf{E}_{\rm sp}|$ (upper-right panel), as well as $n_{\ell,e}$ and holes $n_{j,h}$ (lower panels), as functions of $\Delta\hbar\omega_{\rm sp}$. Here, the results with different energy-level broadening $\hbar\gamma_0 = 3$, 5 and 7 meV are shown in the upper panels, along with a comparison of $n_{\ell,e}$ and holes $n_{j,h}$ for $\hbar\gamma_0 = 3$ and 7 meV in the lower panels.

ative) peak for the probe-field absorption coefficient $\beta_{\rm abs}(\omega_{\rm p})$ due to a quantum coherence effect from the electron states being dressed by an SPP field. In the strong-coupling regime, the dispersion of the quantum-dot e-h plasmas (dot-like branch) and SPPs (photon-like branch) form an anticrossing gap, where a higher-energy dot-like branch at a negative frequency detuning switches to a photon-like branch for a positive detuning. The positive peak is associated with the absorption of a probe-field photon by a quantum-dot e-h plasma, while the negative peak relates to the process with absorption of two photons from an SPP field and emission of one probe-field photon. The absorption peak is significantly reduced by saturation at $E_{\rm sp} = 1000$ kV/cm, and the gain peak is suppressed by a smaller Rabi-coupling frequency at $E_{\rm sp} = 250$ kV/cm (see the inset of the left panel). In addition, we observe from the right panel of Fig. 9 that two Rabi-splitting-induced side emission peaks for the spontaneous emission $P_{\rm em}(\omega)$ become weaker and closer to the strong central peak as $E_{\rm sp}$ is reduced (see the inset of the right panel). Moreover, the strength of the central peak due to the coherent conversion of an absorbed SPP-field photon to a spontaneously-emitted photon (non-linear optical behavior) is slightly reduced at $E_{\rm sp} = 1000$ kV/cm as a result of saturated absorption of the SPP field.

Figure 10 demonstrates the effect of frequency detuning $\Delta\hbar\omega_{\rm sp}$ of an SPP field with respect to the bandgap of a quantum dot. The switching of the detuning from 10 meV to -10 meV reveals the corresponding spectral-position interchange between the absorption (dot-like branch) and the gain (photon-like branch) peaks for $\beta_{\rm abs}(\omega_{\rm p})$ in the left panel of the figure. The Rabi oscillations between the first electron and hole energy levels are weakened with increasing $|\Delta\hbar\omega_{\rm sp}|$. At resonance with a zero detuning, both the absorption and gain peaks are suppressed by very strong Rabi oscillations. This detuning also shifts the emission peaks correspondingly because

#217702 - $15.00 USD Received 23 Jul 2014; accepted 16 Sep 2014; published 30 Oct 2014

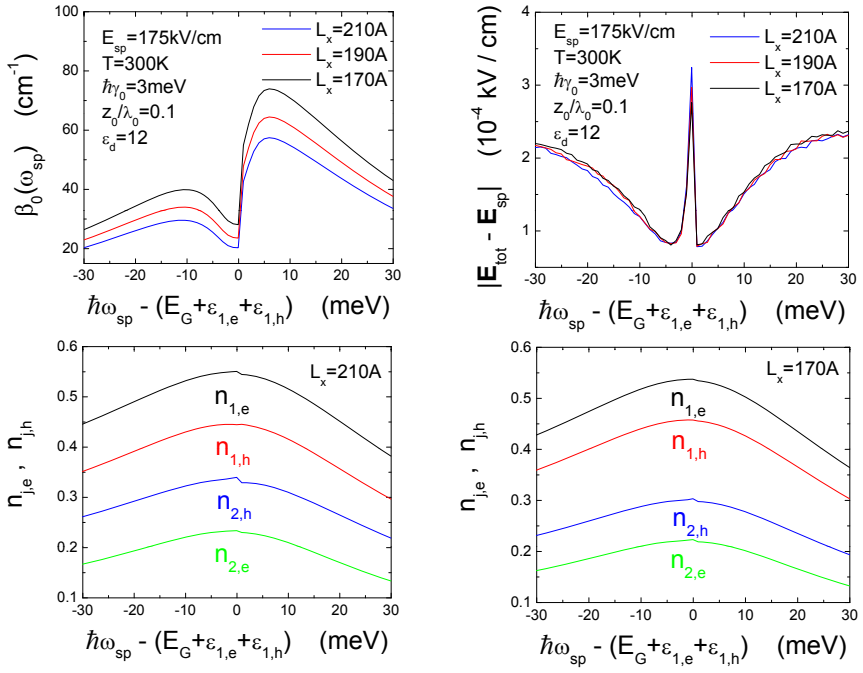

Fig. 6. $\beta_0(\omega_{\rm sp})$ (upper-left panel) and $|\mathbf{E}_{\rm tot}-\mathbf{E}_{\rm sp}|$ (upper-right panel), as well as $n_{\ell,e}$ and holes $n_{j,h}$ (lower panels), as functions of $\Delta\hbar\omega_{\rm sp}$. Here, the results for three different sizes $L_x = 210$, 190 and 170 Å of a quantum dot are shown in the upper panels, along with a comparison of $n_{\ell,e}$ and holes $n_{j,h}$ for $L_x = 210$ and 170 Å in the lower panels.

of the coherent conversion of an SPP-field photon to a spontaneously-emitted one, as can been seen from the right panel of this figure. Moreover, the central peak is weakened and the two side peaks are enlarged at resonance as a result of energy transfer to the side peaks by strong coupling and enhanced Rabi oscillations, respectively.

Since the temperature affects the crystal bandgap energy $E_{\rm G}$, by changing the temperature we are able to scan the detuning $\Delta\hbar\omega_{\rm sp}$ of the SPP field with a fixed SPP frequency $\bar{\hbar}\omega_{\rm sp}$ from negative to positive or vice versa. This leads to a spectral-position interchange between the absorption and gain peaks, similar to Fig. 10. The results in Fig. 11 prove such an expected feature by increasing T from 250 to 300 K in steps of 5 K. Technically, changing the temperature in the experiment is much easier than changing the tuning of a laser frequency over a large range. Here, the shift of the central peak in the right panel of the figure directly reflects the variation of the SPP-field detuning with T. Furthermore, the interchange between the dot-like and photon-like modes with T in the left panel can be regarded as direct evidence for the existence of an anticrossing energy gap resulting from a strongly-coupled e-h plasma and SPP field or coupled e-h plasmas and surface plasmons.

3.3. Time-resolved optical spectra

In our previously presented numerical results, we only showed steady-state dynamics of photo-excited e-h plasmas in a quantum dot by using a continuous SPP field, where the effects of both phonon scattering and e-h pair radiative recombination are combined with each other. Using a laser pulse to launch a pulsed SPP field, we are able to study the dynamics of phonon scattering (narrow pulse) as well as the dynamics of e-h pair radiative recombination (wide

#217702 - $15.00 USD Received 23 Jul 2014; accepted 16 Sep 2014; published 30 Oct 2014

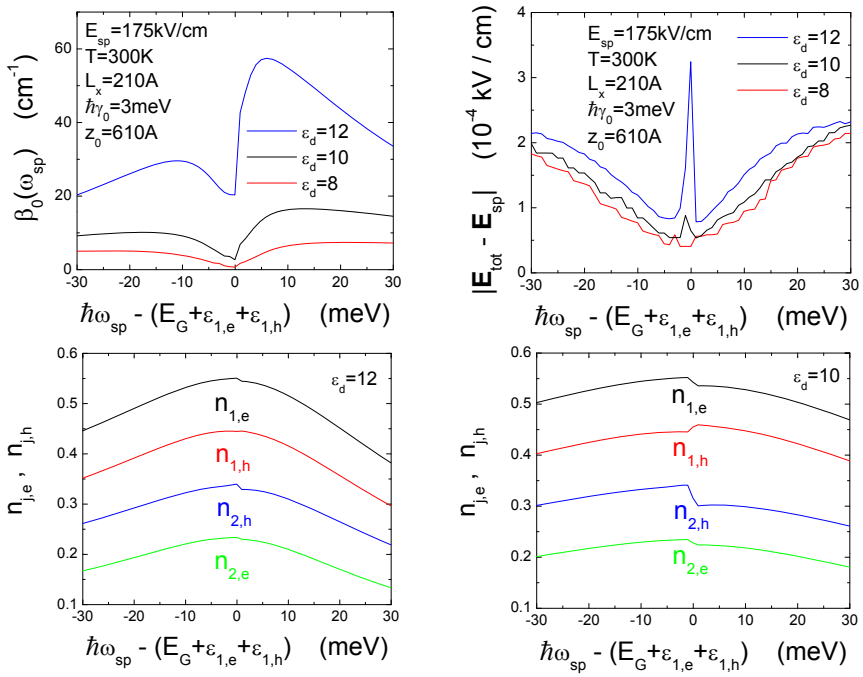

Fig. 7. $\beta_0(\omega_{\rm sp})$ (upper-left panel) and $|\mathbf{E}_{\rm tot}-\mathbf{E}_{\rm sp}|$ (upper-right panel), as well as $n_{\ell,e}$ and holes $n_{j,h}$ (lower panels), as functions of $\Delta\hbar\omega_{\rm sp}$. Here, the results for three dielectric constants of a cladding layer, with $\varepsilon_{\rm d}=8$, 10 and 12, are displayed in the upper panels, along with a comparison of $n_{\ell,e}$ and holes $n_{j,h}$ for $\varepsilon_{\rm d}=12$ and 10 in the lower panels.

pulse), separately. Dynamically, phonon scattering becomes effective only after a characteristic time (around 1 ps), its effect can be seen from a significant increase of $n_{2,\rm e}$ in our system. Figure 12 displays the results for $\beta_0(\omega_{\rm sp})$ (upper-left), $|\mathbf{E}_{\rm tot}-\mathbf{E}_{\rm sp}|$ (upper-right), $n_{1,\rm e}$ (lower-left) and $n_{2,\rm e}$ (lower-right) for various detection times τ_0 in the presence of a narrow laser pulse (with pulse width $T_p=500$ fs and peak value $E_{\rm sp}=500$kV/cm) which is turned on at $t=0$. We see from Fig. 12 that $\beta_0(\omega_{\rm sp})$ starts with a dip for the dressed state at resonance, then shifts to a single peak (at half-pulse width) due to a suppression of the photon-dressing effect. It eventually becomes a single peak plus a shifted dip after the pulse has passed due to formation of resonant peaks in $n_{1,\rm e}$ and $n_{1,\rm h}$. Correspondingly, $|\mathbf{E}_{\rm tot}-\mathbf{E}_{\rm sp}|$ starts by showing a non-resonant behavior with a relatively large magnitude, then shifts to a quasi-resonant behavior, and finally looks like suppressed resonant behavior with a peak at and dips on both sides of $\Delta\hbar\omega_{\rm sp}=0$. The resonant build up of $n_{1,\rm e}$ after $\tau_0\geq 500$ fs can also be verified from this figure, which is accompanied by the start of significant phonon absorption after $\tau_0\geq 1$ ps.

Technically, detecting dynamics of photo-excited e-h plasmas by using another time-delayed weak probe field is much more feasible, as shown in Fig. 13. From the left panel of this figure, we find that $\beta_{\rm abs}(\omega_{\rm p})$ starts with a pair of positive absorption and negative gain peaks due to a very strong photon dressing effect for the delay times $\tau_d=60$ and 120 fs. This is changed to a strong absorption peak plus a very weak gain peak at $\tau_d=240$ fs. At the end, $\beta_{\rm abs}(\omega_{\rm p})$ becomes independent of τ_d, indicating that a linear optical-response regime has been reached. On the other hand, from the right panel of this figure, we see that the central peak of $P_{\rm em}(\omega)$ is gradually built up with increasing τ_d due to enhanced $n_{1,\rm e}$ and $n_{1,\rm h}$ around resonance, while two side peaks become weakened and disappear at the same time due to weakened Rabi oscillations.

#217702 - $15.00 USD Received 23 Jul 2014; accepted 16 Sep 2014; published 30 Oct 2014

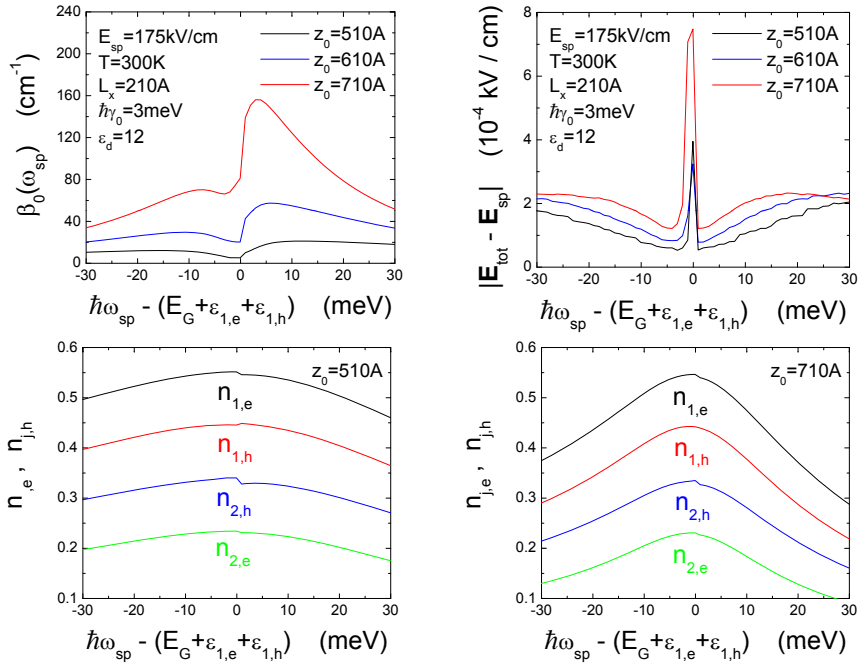

Fig. 8. $\beta_0(\omega_{\rm sp})$ (upper-left panel) and $|\mathbf{E}_{\rm tot}-\mathbf{E}_{\rm sp}|$ (upper-right panel), as well as $n_{\ell,e}$ and holes $n_{j,h}$ (lower panels), as functions of $\Delta\hbar\omega_{\rm sp}$. Here, the results for different vertical distances of a quantum dot from a metallic surface are displayed in the upper panels for $z_0 = 510$, 610 and 710 Å, along with a comparison of $n_{\ell,e}$ and holes $n_{j,h}$ for $z_0 = 510$ and 710 Å in the lower panels.

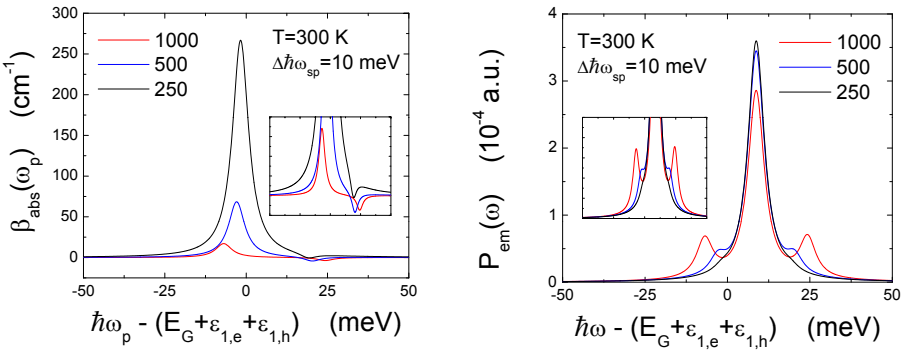

Fig. 9. Probe-field absorption coefficient $\beta_{\rm abs}(\omega_{\rm p})$ (left panel) and spontaneous emission of a quantum dot $P_{\rm em}(\omega)$ (right panel) as functions of $\hbar\omega_{\rm p}-(E_{\rm G}+\varepsilon_{1,\rm e}+\varepsilon_{1,\rm h})$ and $\hbar\omega-(E_{\rm G}+\varepsilon_{1,\rm e}+\varepsilon_{1,\rm h})$, respectively, are presented. Here, comparisons of the results with three values of SPP-field amplitudes $E_{\rm sp} = 250$, 500 and 1000 kV/cm are given. The insets of both panels are enlarged views of the peaks.

#217702 - $15.00 USD Received 23 Jul 2014; accepted 16 Sep 2014; published 30 Oct 2014

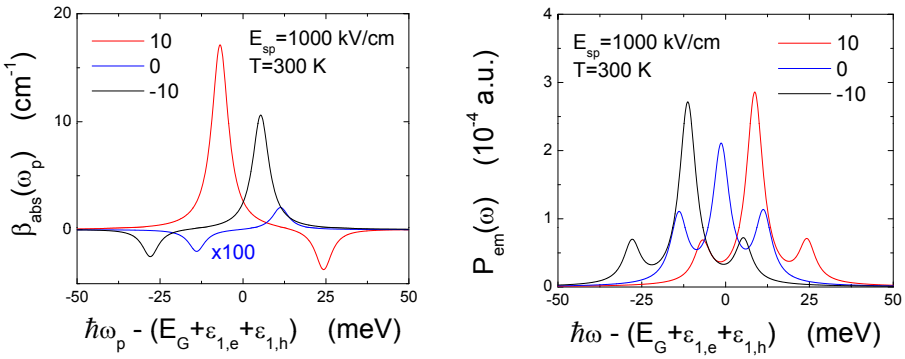

Fig. 10. $\beta_{\rm abs}(\omega_{\rm p})$ (left panel) and $P_{\rm em}(\omega)$ (right panel) as functions of $\hbar\omega_{\rm p}-(E_{\rm G}+\varepsilon_{1,{\rm e}}+\varepsilon_{1,{\rm h}})$ and $\hbar\omega-(E_{\rm G}+\varepsilon_{1,{\rm e}}+\varepsilon_{1,{\rm h}})$, respectively, are displayed. Here, we show the comparisons with three values of SPP-field detunings $\Delta\hbar\omega_{\rm sp}=0$ and ±10 meV. The label $\times100$ for zero SPP-field detuning indicates the result is multiplied by a factor of 100.

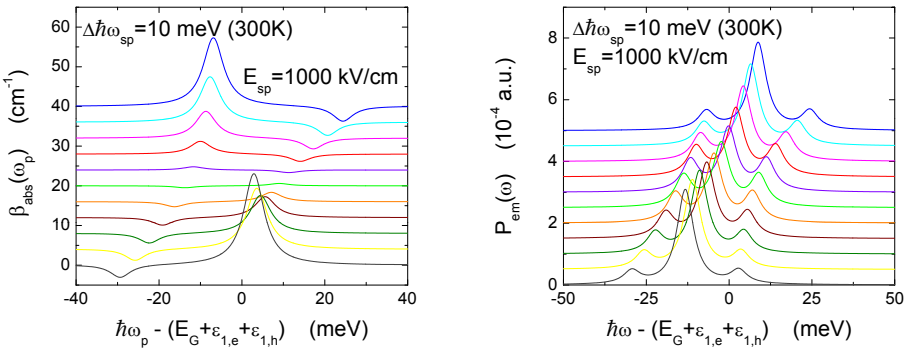

Fig. 11. $\beta_{\rm abs}(\omega_{\rm p})$ (left panel) and $P_{\rm em}(\omega)$ (right panel) as functions of $\hbar\omega_{\rm p}-(E_{\rm G}+\varepsilon_{1,{\rm e}}+\varepsilon_{1,{\rm h}})$ and $\hbar\omega-(E_{\rm G}+\varepsilon_{1,{\rm e}}+\varepsilon_{1,{\rm h}})$, respectively, are shown. Here, a series of offset curves are displayed for various temperatures from $T=250$ K (bottom black curves) to $T=300$ K (top blue curves) in steps of 5 K.

Interestingly, we also find that the central peak of $P_{\rm em}(\omega)$ slightly decreases at $\tau_d=1$ ps, which agrees with the observed start of significant phonon absorption seen in the lower-left panel of Fig. 12.

In order to explore the dynamics of e-h pair radiative recombination in our system, a wide pulse with a full-pulse width around 300 ps is required, as displayed in Fig. 14. From the upper-middle panel of this figure, we find that $\beta_0(\omega_{\rm sp})$ starts with a resonant dip due to a strong photon dressing effect, then shifts to a sole peak at $\Delta\hbar\omega_{\rm sp}=0$ as $\tau_0\geq400$ ps where a steady state is almost reached in the linear-response regime. Accordingly, the level populations $n_{1,{\rm e}}$ and $n_{2,{\rm e}}$ in the lower two panels show a transition from an initial non-resonant behavior to a final resonant behavior. This is accompanied by dramatically reduced level populations due to the start of a radiative recombination process for photo-excited e-h pairs.

Recombination dynamics for e-h plasmas can also be demonstrated clearly by the time-delayed probe-field absorption as well as by the time-resolved spontaneous emission, as shown in Fig. 15. As presented in the left panel of this figure, we find that the initial weak absorption and gain peaks (see the inset) in $\beta_{\rm abs}(\omega_{\rm p})$ occur at $\tau_d=200$ ps and are replaced by a strong single absorption peak due to a suppressed photon dressing effect and phase-space blocking.

#217702 - $15.00 USD Received 23 Jul 2014; accepted 16 Sep 2014; published 30 Oct 2014

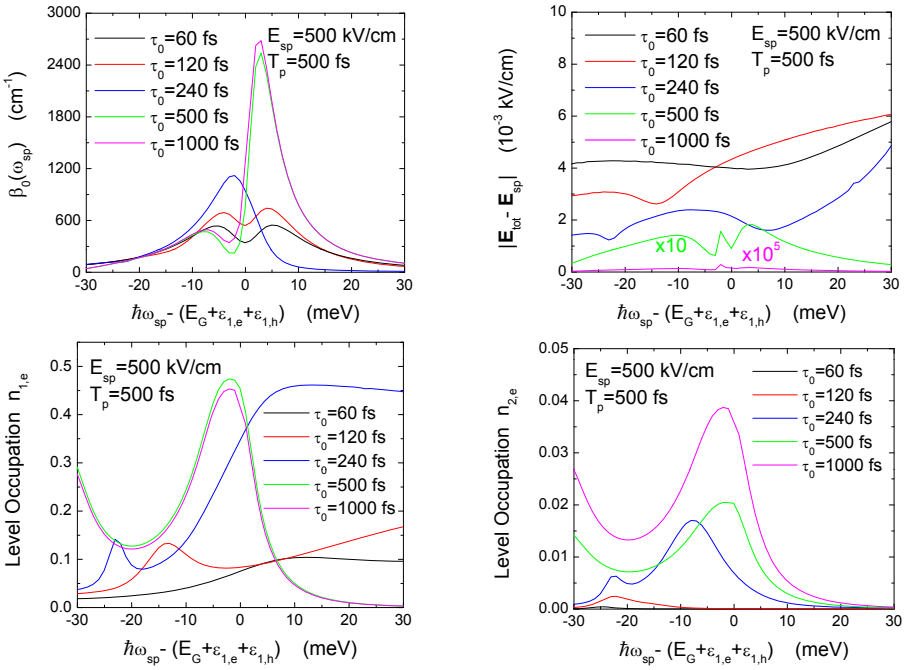

Fig. 12. $\beta_0(\omega_{\rm sp})$ (upper-left panel) and $|\mathbf{E}_{\rm tot}-\mathbf{E}_{\rm sp}|$ (upper-right panel), as well as $n_{1,e}$ and holes $n_{2,e}$ (lower panels), as functions of $\Delta\hbar\omega_{\rm sp}$ at different detection times τ_0 for a Gaussian-shape laser pulse with pulse width $T_p = 500$ fs. Here, $E_{\rm sp} = 500$ kV/cm is taken, and the other parameters are the same as those in Fig. 3. The labels $\times 10$ and $\times 10^5$ in the upper-right panel indicate that the results are multiplied by factors of 10 and 10^5, respectively.

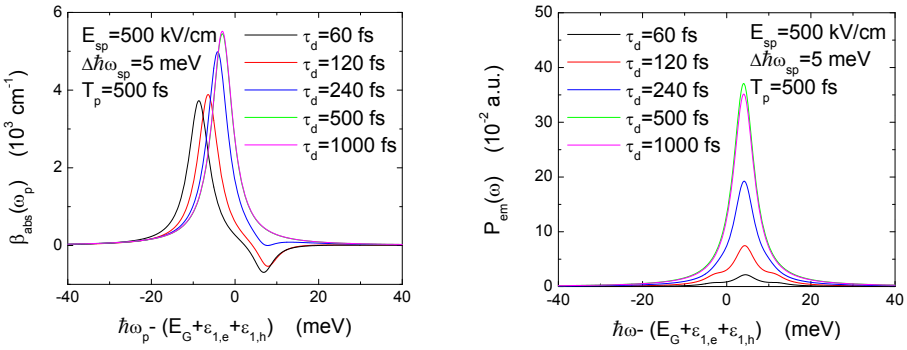

Fig. 13. $\beta_{\rm abs}(\omega_{\rm p})$ (left panel) and $P_{\rm em}(\omega)$ (right panel) as functions of $\hbar\omega_{\rm p} - (E_{\rm G} + \varepsilon_{1,{\rm e}} + \varepsilon_{1,{\rm h}})$ and $\hbar\omega - (E_{\rm G} + \varepsilon_{1,{\rm e}} + \varepsilon_{1,{\rm h}})$, respectively, at different delay times τ_d for a Gaussian-shape laser pulse with pulse width $T_p = 500$ fs. Here, $E_{\rm sp} = 500$ kV/cm and $\Delta\hbar\omega_{\rm sp} = 5$ meV are chosen, and the other parameters are the same as those in Fig. 3.

#217702 - $15.00 USD Received 23 Jul 2014; accepted 16 Sep 2014; published 30 Oct 2014

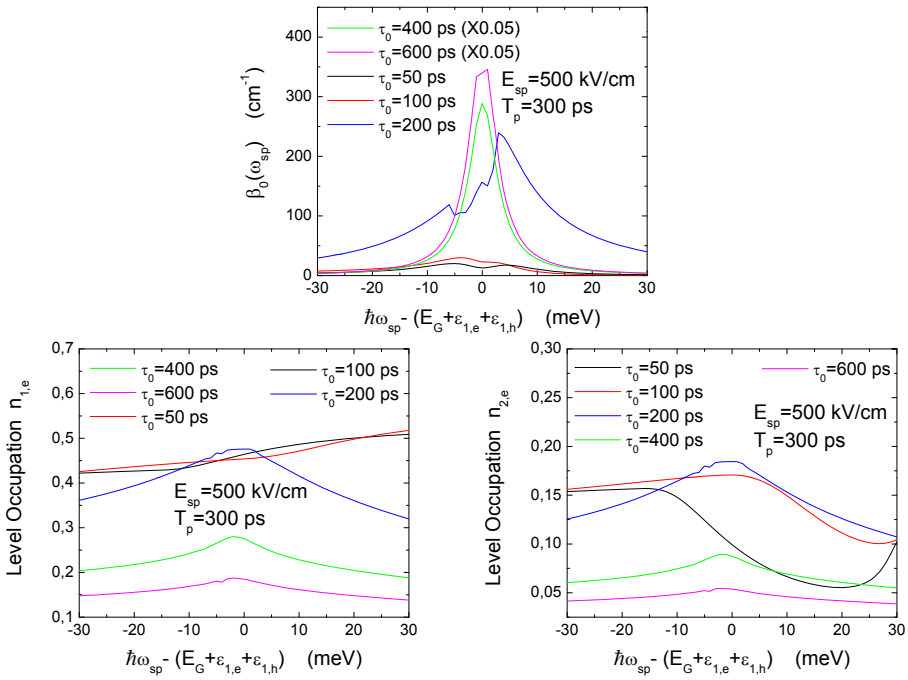

Fig. 14. $\beta_0(\omega_{\rm sp})$ (upper-middle panel), $n_{1,e}$ and holes $n_{2,e}$ (lower two panels), as functions of $\Delta\hbar\omega_{\rm sp}$ at different detection times τ_0 for a wide laser pulse with pulse width $T_p = 300$ ps. Here, $E_{\rm sp} = 500$ kV/cm is taken, and the other parameters are the same as those in Fig. 3. The labels $\times 0.05$ in the upper-middle panel indicate that the results in the upper panel for $\tau_0 = 60$ and 120 ps are multiplied by a factor of 0.05.

On the other hand, from the right panel of the same figure, we see that the initial central peak in $P_{\rm em}(\omega)$ is increased very rapidly due to accumulation of photo-excited e-h pairs and accompanied by the reduction of two side peaks resulting from the weakened Rabi oscillations. Importantly, the very-strong central peak in $P_{\rm em}(\omega)$ is significantly reduced at $\tau_d = 200$ ps, indicating the start of a radiative-recombination process for photo-excited e-h plasmas. This recombination process is continuously enhanced with the increasing delay time τ_d and suppresses the central peak in $P_{\rm em}(\omega)$ after $\tau_d \geq 400$ ps due to draining out the photo-generated electrons and holes at the same time.

4. Conclusions and remarks

In conclusion, we have demonstrated the possibility of using a SPP field to control the optical gain and absorption of another passing light beam due to their strong nonlinear field coupling mediated by electrons in the quantum dot. We have also predicted the coherent conversion of a surface-plasmon-field photon to a spontaneously-emitted free-space photon, which is simultaneously accompanied by another pair of blue- and red-shifted photons.

Although we studied only the coupling of a SPP field to a single quantum dot in this paper for the simplest case, our formalism can be generalized easily to include many quantum dots. The numerically-demonstrated unique control of the effective photon-photon coupling by the quantum dot can be used for constructing an optical transistor, where the 'gate' photon controls the intensity of its 'source' light beam. These optical transistors are very useful for speeding up and improving the performance of fiber-optic communication networks, as well as for constructing

#217702 - $15.00 USD Received 23 Jul 2014; accepted 16 Sep 2014; published 30 Oct 2014

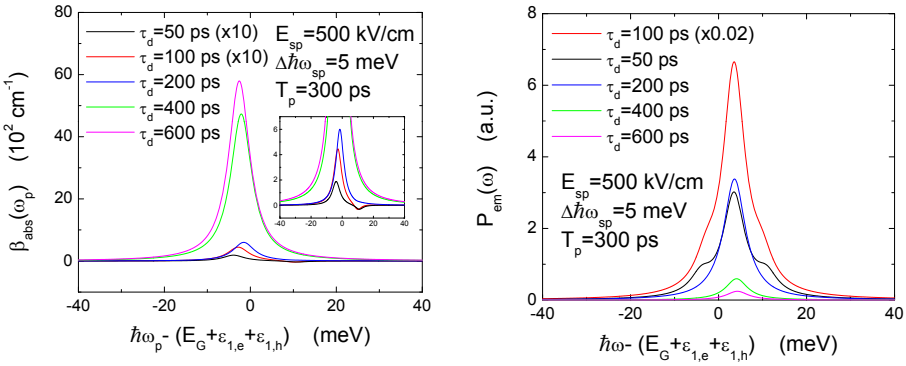

Fig. 15. $\beta_{\rm abs}(\omega_{\rm p})$ (left panel) and $P_{\rm em}(\omega)$ (right panel) as functions of $\hbar\omega_{\rm p}-(E_{\rm G}+\varepsilon_{1,{\rm e}}+\varepsilon_{1,{\rm h}})$ and $\hbar\omega-(E_{\rm G}+\varepsilon_{1,{\rm e}}+\varepsilon_{1,{\rm h}})$, respectively, at different delay times τ_d for a Gaussian-shape laser pulse with pulse width $T_p=300$ ps. Here, $E_{\rm sp}=500$ kV/cm and $\Delta\hbar\omega_{\rm sp}=5$ meV are assumed, and the other parameters are the same as those in Fig. 3. The inset in the upper-left panel shows an enlarged view for the gain and absorption peaks for small delay times. The labels $\times 10$ for $\tau_d=50$ and 100 ps in the left panel, as well as the label $\times 0.02$ in the right panel, indicate that the results are multiplied by a factor of 10 and a factor of 0.02, respectively.

quantum information and developing optical digital computers.

Furthermore, instead of a resonant coupling to the lowest pair of electron-hole energy levels, we may select the surface-plasmon frequency for resonant coupling to the higher pair of electron-hole levels. In such a case, the optical pumping from the intense surface-plasmon near-field could create a population inversion with respect to the ground pair of electron-hole levels by emitting thermal phonons, leading to a possible lasing action if the optical gain can overcome the metal loss for the surface plasmons. Such a surface-plasmon quantum-dot laser would have a beam size as small as a few nanometers beyond the optical diffraction limit, and it is expected to be very useful for spatially-selective illumination of individual molecules or neuron cells in low-temperature photo-excited chemical reactions or optogenetics and neuroscience.

A. Results Related to the Electronic States of a Quantum Dot

We have employed a box-type potential with hard walls to model a quantum dot, which is given by

$$V(\mathbf{r})=\begin{cases} 0\,, & 0\le x_i\le L_i \text{ for } i=1,2,3 \\ \infty\,, & \text{otherwise}\end{cases}\,, \tag{73}$$

where the position vector $\mathbf{r}=(x_1,x_2,x_3)$, and L_1, L_2 and L_3 are the widths of the potential in the x_1, x_2 and x_3 directions, respectively. The Schrödinger equation for a single electron or hole in a quantum dot is written as

$$-\frac{\hbar^2}{2m^*}\left[\frac{\partial^2}{\partial x_1^2}+\frac{\partial^2}{\partial x_2^2}+\frac{\partial^2}{\partial x_3^2}+V(\mathbf{r})\right]\psi(\mathbf{r})=\varepsilon\,\psi(\mathbf{r})\,, \tag{74}$$

where the effective mass m^* is $m_{\rm e}^*$ for electrons or $m_{\rm h}^*$ for holes. The eigenstate wave-function associated with Eq. (74) is found to be

#217702 - $15.00 USD Received 23 Jul 2014; accepted 16 Sep 2014; published 30 Oct 2014

$$\psi_{n_1,n_2,n_3}(\mathbf{r}) = \sqrt{\frac{2}{L_1}}\sin\left[\left(\frac{n_1\pi}{L_1}\right)x_1\right]\sqrt{\frac{2}{L_2}}\sin\left[\left(\frac{n_2\pi}{L_2}\right)x_2\right]\sqrt{\frac{2}{L_3}}\sin\left[\left(\frac{n_3\pi}{L_3}\right)x_3\right], \quad (75)$$

which is same for both electrons and holes, and the eigenstate energy associated with Eq. (74) is

$$\varepsilon_{n_1,n_2,n_3} = \frac{\hbar^2}{2m^*}\left[\left(\frac{n_1\pi}{L_1}\right)^2 + \left(\frac{n_2\pi}{L_2}\right)^2 + \left(\frac{n_3\pi}{L_3}\right)^2\right], \quad (76)$$

where the quantum numbers $n_1, n_2, n_3 = 1, 2, \cdots$.

By using the calculated bare energy levels in Eq. (76), the dressed electron ($\lambda_\alpha^{\rm e}$) and hole ($\lambda_\alpha^{\rm h}$) energy levels under the rotating wave approximation take the forms [2]

$$\lambda_\alpha^{\rm e}(\omega|t) = \lambda_\alpha^{\rm h}(\omega|t) = \begin{cases} \frac{1}{2}\left(\hbar\omega + \sqrt{[\mathscr{E}_{\rm G}(T) + \varepsilon_\alpha^{\rm e} + \varepsilon_\alpha^{\rm h} - \hbar\omega]^2 + 4|\mathscr{M}_{\alpha,\alpha}^{\rm eh}(t)|^2}\right) \\ \qquad \text{if } \hbar\omega \le \mathscr{E}_{\rm G}(T) + \varepsilon_\alpha^{\rm e} + \varepsilon_\alpha^{\rm h} \\ \frac{1}{2}\left(\hbar\omega - \sqrt{[\mathscr{E}_{\rm G}(T) + \varepsilon_\alpha^{\rm e} + \varepsilon_\alpha^{\rm h} - \hbar\omega]^2 + 4|\mathscr{M}_{\alpha,\alpha}^{\rm eh}(t)|^2}\right) \\ \qquad \text{if } \hbar\omega \ge \mathscr{E}_{\rm G}(T) + \varepsilon_\alpha^{\rm e} + \varepsilon_\alpha^{\rm h} \end{cases}, \quad (77)$$

where the composite index $\alpha = \{n_1, n_2, n_3\}$. Moreover, we obtain the energy levels of dressed electrons $\overline{\varepsilon}_\alpha^{\rm e}(\omega|t) = \lambda_\alpha^{\rm e}(\omega|t) + (\varepsilon_\alpha^{\rm e} - \varepsilon_\alpha^{\rm h})/2$ and $\overline{\varepsilon}_\ell^{\rm e}(\omega|t) = \varepsilon_\ell^{\rm e} + \mathscr{E}_{\rm G}(T)/2$ for $\ell \neq \alpha$. Similarly, we obtain the energy levels of dressed holes $\overline{\varepsilon}_\alpha^{\rm h}(\omega|t) = \lambda_\alpha^{\rm h}(\omega|t) + (\varepsilon_\alpha^{\rm h} - \varepsilon_\alpha^{\rm e})/2$ and $\overline{\varepsilon}_j^{\rm e}(\omega|t) = \varepsilon_j^{\rm h} + \mathscr{E}_{\rm G}(T)/2$ for $j \neq \alpha$.

Based on the calculated wave-functions in Eq. (75), the form factors introduced in Eqs. (11) and (12) can be obtained from

$$\mathscr{F}_{n_1,n_2,n_3;n_1',n_2',n_3'}^{\rm e}(\mathbf{q}) = \mathscr{F}_{n_1,n_2,n_3;n_1',n_2',n_3'}^{\rm h}(\mathbf{q}) = \mathscr{Q}_{n_1,n_1'}^{(1)}(q_1)\,\mathscr{Q}_{n_2,n_2'}^{(2)}(q_2)\,\mathscr{Q}_{n_3,n_3'}^{(3)}(q_3), \quad (78)$$

where the wave vector $\mathbf{q} = (q_1, q_2, q_3)$ and we have introduced the following notation for $j = 1, 2, 3$

$$\mathscr{Q}_{n_j,n_j'}^{j}(q_j) = \left(\frac{2}{L_j}\right)\int_0^{L_j} dx_j\, {\rm e}^{iq_jx_j}\sin\left[\left(\frac{n_j\pi}{L_j}\right)x_j\right]\sin\left[\left(\frac{n_j'\pi}{L_j}\right)x_j\right]. \quad (79)$$

Moreover,the overlap of the electron and hole wave-functions in this model can be easily calculated as

$$\int d^3\mathbf{r}\,\psi_{n_1,n_2,n_3}^{\rm e}(\mathbf{r})\,\psi_{n_1',n_2',n_3'}^{\rm h}(\mathbf{r}) = \delta_{n_1,n_1'}\,\delta_{n_2,n_2'}\,\delta_{n_3,n_3'}. \quad (80)$$

The interband dipole moment $\mathbf{d}_{\rm c,v} = d_{\rm c,v}\,\hat{\mathbf{e}}_{\rm d}$ at the isotropic Γ-point, which is defined in Eq. (32), can be calculated according to the Kane approximation [35, 36]

$$d_{\rm c,v} = \sqrt{\frac{e^2\hbar^2}{2m_0\,\mathscr{E}_{\rm G}(T)}\left(\frac{m_0}{m_{\rm e}^*} - 1\right)}. \quad (81)$$

Furthermore, the direction of the dipole moment $\hat{\mathbf{e}}_{\rm d}$ is determined by the quantum-dot energy levels in resonance with the photon energy $\hbar\omega$.

#217702 - $15.00 USD Received 23 Jul 2014; accepted 16 Sep 2014; published 30 Oct 2014

Acknowledgments

DH would like to thank the Air Force Office of Scientific Research (AFOSR) for support. GG was supported by contract # FA 9453-13-1-0291 of AFRL.

#217702 - $15.00 USD Received 23 Jul 2014; accepted 16 Sep 2014; published 30 Oct 2014